学位論文

Photoemission study of the iron-based superconductor
FeTe$_{1-x}$Se$_x$

（鉄系超伝導体 FeTe$_{1-x}$Se$_x$の光電子分光による研究）

平成２５年１２月博士（理学）申請

東京大学大学院理学系研究科
物理学専攻

レオ クリストバル カストロ アンボローデ Ⅱ
Leo Cristobal Castro AMBOLODE II

Photoemission study of the iron-based superconductor $FeTe_{1-x}Se_x$

Doctor Thesis

Leo Cristobal Castro Ambolode II

Department of Physics

Faculty of Science & Graduate School of Science

THE UNIVERSITY OF TOKYO

December 2013

Abstract

Since the discovery of the iron-based superconductor fluorine-doped LaFeAsO with a T_c of 26 K, a lot of effort have been poured out trying to understand the mechanism of the superconductivity in this new type of high-T_c materials. It also drives the scientific community to synthesize new superconductors with higher T_c's. Among the iron-based high-T_c superconductors, the binary 11 family of $Fe_{1+y}Te_{1-x}Se_x$, having the simplest crystal structure, offers the possibility of providing valuable information about the origin of superconductivity in iron-based superconductors.

This research sought to investigate the electronic structure and to elucidate the strength of electron correlation in the simplest kind of iron-based superconductor, the $Fe_{1+y}Te_{1-x}Se_x$ system. For the first part, we carried out resonance photoemission experiments on the compounds, $x = 0, 0.4$ single crystals and polycrystalline FeSe ($x = 1$) samples, using photon energies in the Fe $3p \rightarrow 3d$ absorption region. We found out that, like most of the other iron-based superconductors, the density of states near the Fermi level down to the binding energy of around 2 eV is mostly dominated by the Fe $3d$ states. We also found out that the Fe $3p \rightarrow 3d$ resonance occurs at $hv \sim 55$ eV and we were able to deduce the Fe $3d$ partial density of states (PDOS) for all the samples. The near E_F peak structure in FeSe, splits into two features in compounds with Te content. By comparing the PDOS with angle-resolved photoemission (ARPES) results, the peak structure can be attributed to the dominant Fe $3d_{z^2}$ states. We obtained the mass renormalization factor of around 2 for d_{z^2}, which shows moderate electron correlation consistent with the band calculation and previous photoemission results.

For the second part, we performed high-resolution ARPES measurements for the single crystals $Fe_{1+y}Te_{1-x}Se_x$ ($x = 0, 0.1, 0.2, 0.4$). Near

the Fermi level, three band dispersions were clearly observed around the Γ point. Mass renormalization factors obtained from the photoemission measurements for different bands are consistent with the calculation and resolved inconsistencies found in previous experimental data. Our results further confirm the strong orbital dependence of the mass renormalization factor in iron chalcogenides and have shown that $Fe_{1+y}Te_{1-x}Se_x$ is a strongly correlated compound different from other iron-based superconductors. The d_{xy} band is the most strongly correlated with a mass renormalization factor of around 10, while the d_{yz} and d_{xz} bands show moderate electron correlations with mass renormalization factors of around 1.5 - 2. As for the composition dependence, only the d_{xz} band exhibits strong Se concentration dependence (chalcogen height-dependence) evident in the band shift, while the d_{yz} and d_{xy} bands did not show any significant change in the band position, nor in the mass renormalization factor or strength of electron correlation. The band shift of the d_{xz} orbital is due to its strong dependence on the chalcogen height as well as on the k_z dispersion especially around the k_z values relevant to our study.

In conclusion, using photoemission spectroscopy, which is a powerful tool to investigate the electronic structure of solids, we have found that the simplest iron-based superconductor $Fe_{1+y}Te_{1-x}Se_x$ is a strongly correlated material different from other iron-based superconductors. The unusually large orbital differentiation of mass renormalization factor for this compound, particularly for FeTe, and the dominant contribution of the largely enhanced d_{xy} band on the Fermi surface are possible contributing factors for the suppression of superconductivity on this compound.

Table of Contents

Chapter 1

Introduction

1.1 Overview

In 1908, a Dutch physicist Heike Kamerlingh Onnes successfully liquefied helium that allowed him to study physical properties of materials at temperatures just a few degrees above the absolute zero [1]. Three years later, he discovered the phenomenon of superconductivity when he found that the dc resistivity of mercury suddenly drops to zero below 4.2 K [2]. However, this phenomenon remained confined to very low temperatures until the real history of high-T_c superconductivity began in 1986 when Bednorz and Müller found evidence for superconductivity at 30 K in LaBaCuO ceramics [3]. This remarkable discovery has renewed the interest in superconductivity research and soon after that, many related materials which came to be known as cuprates were discovered to show superconductivity at high-T_c values until the highest critical T_c = 135 K was achieved in 1993 in Hg-based cuprates (T_c = 164 K at high pressure). The history of superconducting materials with their corresponding critical temperatures is shown in Fig. 1.1. After twenty-two years of dominance of cuprates in the field of high-T_c superconductivity research, a new class of compounds known as iron pnictides [4] were discovered and opened a new route for the high-T_c superconductivity research in addition to that of the cuprates. This new class of iron-based systems shares some common properties with cuprates such as the layered crystal structures and antiferromagnetic (AFM) ordering in the parent compounds, however, many differences exist between the two classes especially in their electronic structures.
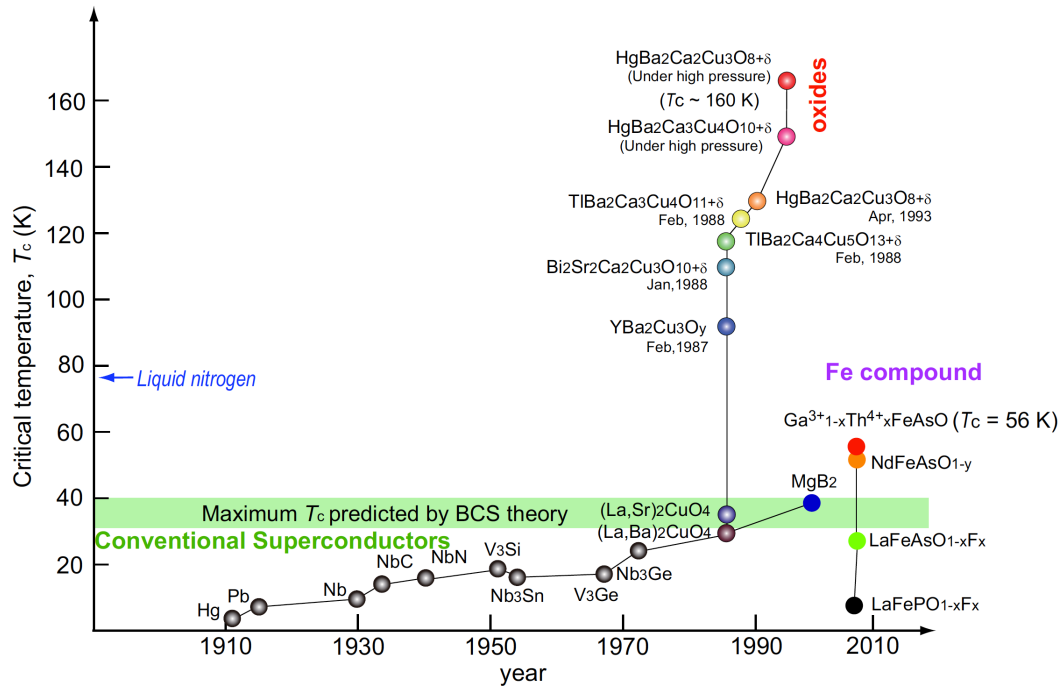
Figure 1.1: Critical temperature T_c showing the history of superconductivity (Courtesy of S. Ideta). Superconductivity was first found in Hg in 1911.

1.2 Strongly Correlated Systems

High-T_c superconductors belong to a large class of materials, namely, strongly correlated materials, which are characterized by strong interactions or correlations between electrons. The history of strongly correlated material began in the early days of modern solid state physics. In the 1930's, Bloch [5] and Wilson [6] developed band theory, which explained why some materials exhibit metallic behavior and others insulating. Soon after, Boer and Verweij pointed out that the band theory failed for a large number of insulating $3d$ transition metal compounds, such as NiO and CoO, which were predicted to be metals [7]. Peierls suggested that the strong local d-d Coulomb interaction between electrons overcame the energy gain by delocalization of the electrons.

Mott and Hubbard also suggested that the insulating behavior is attributed to electron-electron correlation [8-10]. Nowadays, the Hubbard model is frequently used to study strong correlated system. In the meantime, Anderson introduced super-exchange in a model with strong d-d Coulomb interaction of local $3d$ electrons caused by the energy lowering via hopping [11, 12]. This model is virtually identical to the Hubbard model.

It is well known that strong electron correlation plays a major role in the cuprate superconductors. For the iron-based superconductors, a general belief based on experimental data and from calculation is that these materials show less degree of electron correlations than cuprates [13]. However, it is still far from being well understood as to how electron correlations affect the mechanism that leads to superconductivity in this new class of superconducting materials.

1.3 Outline of thesis

This dissertation is organized as follows. In Chapter 2, I present an overview of the high T_c superconductivity particularly on iron-based superconductors. I describe the physical and electronic properties of the iron-based superconductors in this chapter, focusing mainly on the iron chalcogenides. In Chapter 3, I briefly review the fundamental concepts involved in photoelectron spectroscopy. The instrumentation and experimental details will also be discussed in this chapter.

The main objective of my research is to investigate the electronic structure and the strength of electronic correlations in the simplest iron-based superconductor, namely, the 11 systems, using photoemission spectroscopy. I present the angle-integrated and angle-resolved photoemission results of

$Fe_{1+y}Te_{1-x}Se_x$ system in Chapters 4 and 5, respectively. For comparison, I mention important experiments and theoretical works every now and then. Finally, I give my conclusion in Chapter 6.

Chapter 2

Brief review of iron-based superconductors

Since the discovery of the iron-based superconductor fluorine-doped LaFeAsO with a T_c of 26 K by Hideo Hosono and collaborators in February 2008 [4], a lot of efforts have been poured out trying to understand the mechanism of superconductivity in this new type of high-T_c materials. This surprising discovery of superconductivity in layered materials and the interesting physical properties of Fe-based superconductors made the beginning of worldwide efforts to investigate this new family of superconductors and have led to thousands of publications on this subject over the past few years. Historically, the seemingly antagonistic relationship between superconductivity and magnetism has led researchers not to use magnetic elements, ferromagnetic in particular, as potential building blocks of new superconducting materials. Since iron element is strongly magnetic, the discovery of Fe-based superconductors with high T_c values was completely unexpected. In this chapter, I will briefly review of what has been done and understood so far in this new type of high-T_c superconductors. But since my research is only focused on the 11 systems, I will discuss more on this type of iron-based superconductor.

2.1 Crystal structure of iron-based superconductors

So far, five unique crystallographic structures have been reported to show superconductivity. All of these materials share the same basic structure, tetragonal symmetry at room temperature and range from the simplest α-PbO-type binary element structure to more complicated quinternary structures composed of elements that span the entire periodic table [14, 15].

1111 family

Following the discovery of high-T_c superconductivity in LaFeAsO$_{1-x}$F$_x$, T_c rapidly increased by exchanging lanthanum with rare earth ions of smaller atomic radii in LnFeAsO and appropriate carrier doping or creating oxygen deficiencies, until it reached a maximum value of $\sim$ 56 K in Gd$_{1-x}$Th$_x$FeAsO [16]. This family of LnFeAsO is known as 1111 family. LaFeAsO and the 1111 family of iron pnictides crystallizes in the ZrCuSiAs-type structure, (space group P4/nmm). In this structure, two-dimensional layers of edge-sharing FeAs$_4$/4 tetrahedra alternate with sheets of edge-sharing OLa$_4$/4 tetrahedra as shown in Fig. 2.1 (a). Because of the differences between the ionic nature of the Ln-O (Lanthanum oxide) bonds and the more covalent Fe-As (iron arsenide) bonds, a distinctive two-dimensional structure forms, where ionic layers of lanthanum oxide (LaO)$^+$ alternate with metallic layers of iron arsenide (FeAs)$^-$.

122 family

M. Rotter et al. [17] proposed BaFe$_2$As$_2$ as a potential new parent compound based on the similarities between BaFe$_2$As$_2$ and LaFeAsO. In fact, both compounds contain identical FeAs layers, and have the same charge accordance as follows: Ba^{2+}[(FeAs)$^-$]^2 vs. (LaO)$^+$(FeAs)$^-$. Partial replacement

of Barium with Potassium (hole doping) induced superconductivity at 38 K in $Ba_{0.6}K_{0.4}Fe_2As_2$ [18], the first member of a new family of superconducting iron arsenides known as the 122 family. The ternary iron arsenide $BaFe_2As_2$, with the tetragonal $ThCr_2Si_2$-type structure space group (space group I4/nmm) contains practically identical layers of edge-sharing $FeAs_4/4$ tetrahedra, but they are separated by barium atoms instead of LaO sheets. This structure is shown in Fig. 2.1(b) [18].

111 family

X. C. Wang et al. [19] reported the discovery of another new superconducting iron arsenide system LiFeAs (termed 111). Superconductivity with Tc up to 18 K was found in these compounds. LiFeAs crystallizes into a Cu_2Sb-type tetragonal structure containing FeAs layer with an average iron valence Fe^{2+} like those for 1111 or 122 parent compounds. This structure is shown in Fig. 2.1(c) [19].

11 family

F.-C. Hsu et al. [20] reported the observation of superconductivity with zero resistance transition temperature at 8 K in the PbO-type αFeSe compound known as 11 family. Although FeSe has been studied quite extensively, a key observation is that the clean superconducting phase exists only in those samples prepared with intentional Se deficiency. The PbO-type αFeSe crystal structure is shown in Fig. 2.1 (d) [20].

42622 family

X. Zhu *et al.* successfully fabricated the superconducting $Sr_4V_2O_6Fe_2As_2$ compound with a transition temperature of 37.2 K [21]. It has a layered structure with the space group of P4/nmm, and shows more complicated perovskite-like combinations as shown in Fig. 2.1(e).
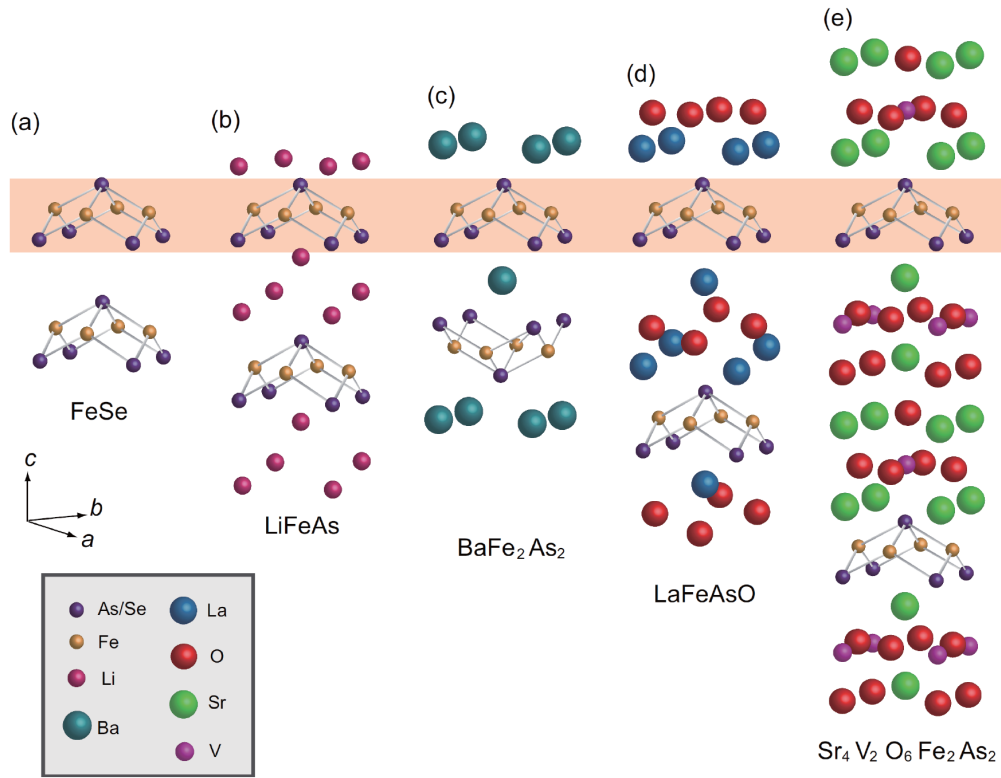
Figure 2.1: Crystallographic structure of the iron-based superconductors (Courtesy of S. Ideta). (a)-(e): The five tetragonal structures with their representative compounds that have been known to show superconductivity. FeAs/FeSe layers are shown in the shaded region.

2.2 $Fe_{1+y}Te_{1-x}Se_x$ family

2.2.1 Phase diagram

Katayama *et al*. [22] have investigated the phase diagram of $Fe_{1+y}Se_xTe_{1-x}$ compounds using bulk magnetization techniques. Using bulk susceptibility data obtained from the single crystal samples, they were able to produce the phase diagram of $Fe_{1+y}Se_xTe_{1-x}$, as shown in Fig. 2.2. Even though the values of x and y are nominal values and may not be exactly correct, the phase diagram clearly shows the trends and the existence of three distinct phases; the antiferromagnetic phase for $x \leq 0.1$, the bulk superconducting phase for $x \leq 0.4$, and the intermediate spin-glass phase.
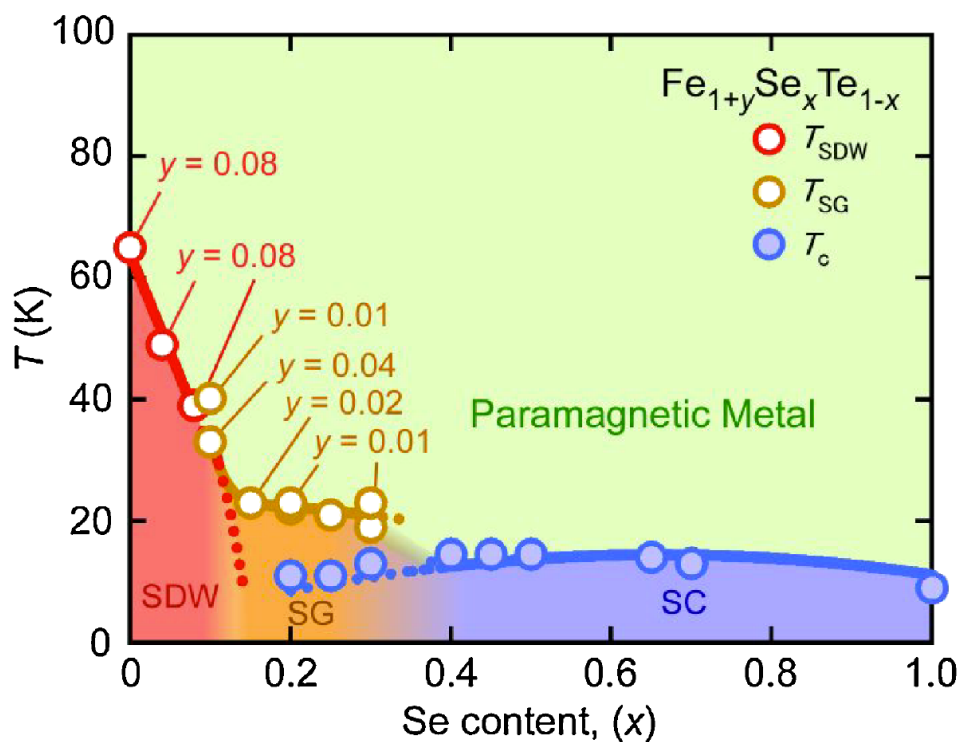
Fig. 2.2: Phase diagram of $Fe_{1+y}Te_{1-x}Se_x$ as a function of Se content x and temperature T with the excess Fe $y \sim 0$ [22].

2.2.2 Electronic structure

In order to understand the bulk electronic properties, it is important to determine the electronic structure. The electronic structure for the 11 systems is shown in Fig. 2.3. These results are generally similar with the other iron-based superconductors. In particular, all the compounds show small compensating electron and hole Fermi surfaces at the zone corner and center, respectively, but high density of states (DOS).
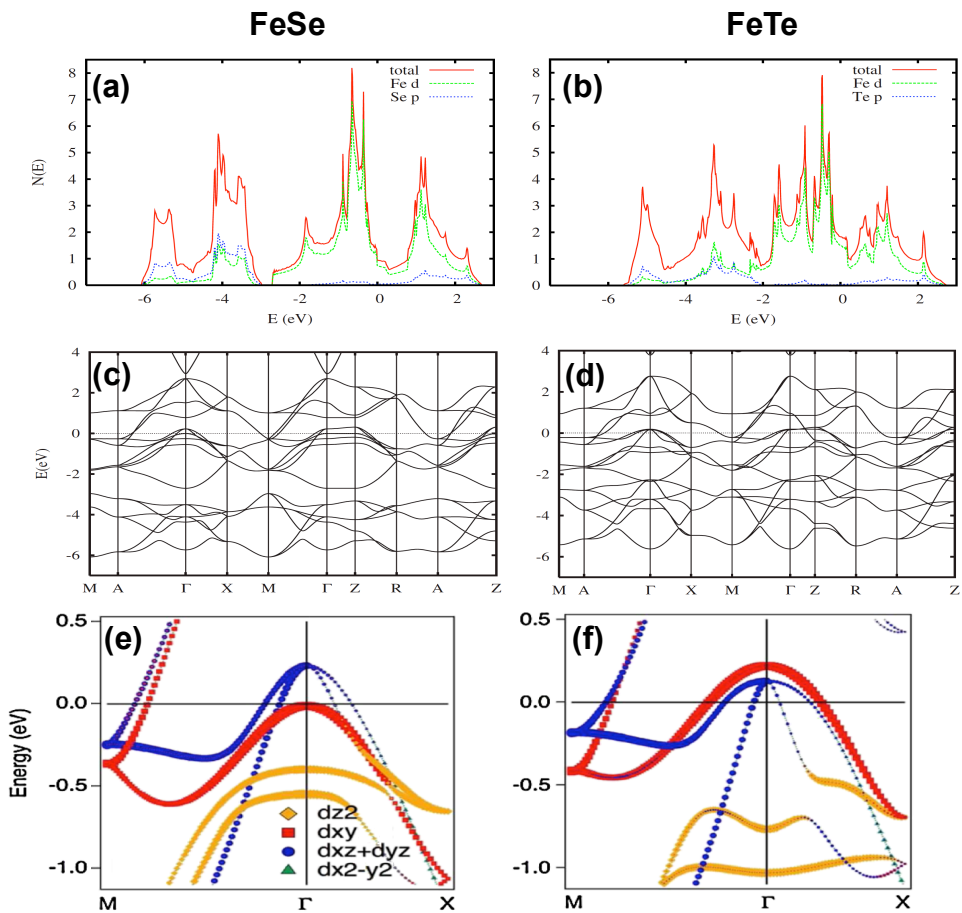
Figure 2.3: (a), (b) Electronic DOS and (c), (d) band structure calculation for FeSe and FeTe, respectively [23]. (e), (f) Near-E_F band structure for FeSe and FeTe, respectively [24]. Reprinted with permission from Refs. [23] and [24]. © (2008) and (2010), respectively, by the American Physical Society.

2.2.3 Mass renormalization

The iron-based superconductors are generally believed to show less degree of correlation as compared to cuprates. The mass renormalization for various iron-based materials were calculated by Yin *et al*. [13] using the dynamical mean field theory + density functional theory (DMFT + DFT). Most of the materials show moderate electron correlation except for the 11 systems, which show relatively large values. In addition, the 11 systems also exhibit strong orbital dependence of the mass renormalization, which is strongest in FeTe.
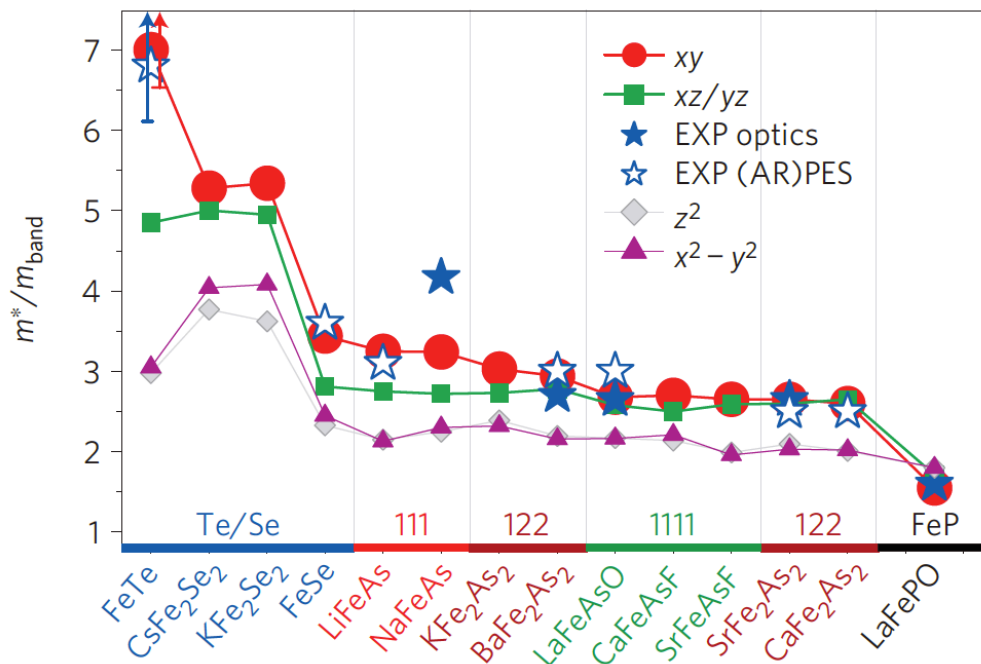
Figure 2.4: Orbital dependent mass renormalization values of various iron-based superconductors estimated from DMFT + DFT calculation. Experimental data marked with stars are also included in the plot. Reprinted by permission from Macmillan Publishers Ltd: Nature Materials [13] © (2011).

2.2.4 Previous ARPES results

A number of angle-resolved photoemission spectroscopic (ARPES) studies have been done on the 11 family of iron-based materials, particularly the $Fe_{1+y}Te_{1-x}Se_x$ systems, is shown in Fig. 2.5. Depending on the Se content (or Te content), x, the experimental data have shown varied electronic structure. Some experiments have found three band dispersions around the Γ point while others found only two. The band dispersions usually differ in energy scale from the calculated bands. Such difference in energy scale can be accounted for by the electron correlation through mass renormalization. Tabulated in Table 2.1 are the mass renormalization obtained from ARPES for various compositions. The mass renormalization varies greatly with composition with values ranging from about 2 and could reach as high as 17. However, the variation is not systematic with respect to Se content. Another thing is the strong orbital dependence of the mass renormalization evident in Tamai *et al*. [24] and Maletz *et al*. [29] results. Nevertheless, these results reveal the strong dependence of the electronic structure on the composition.
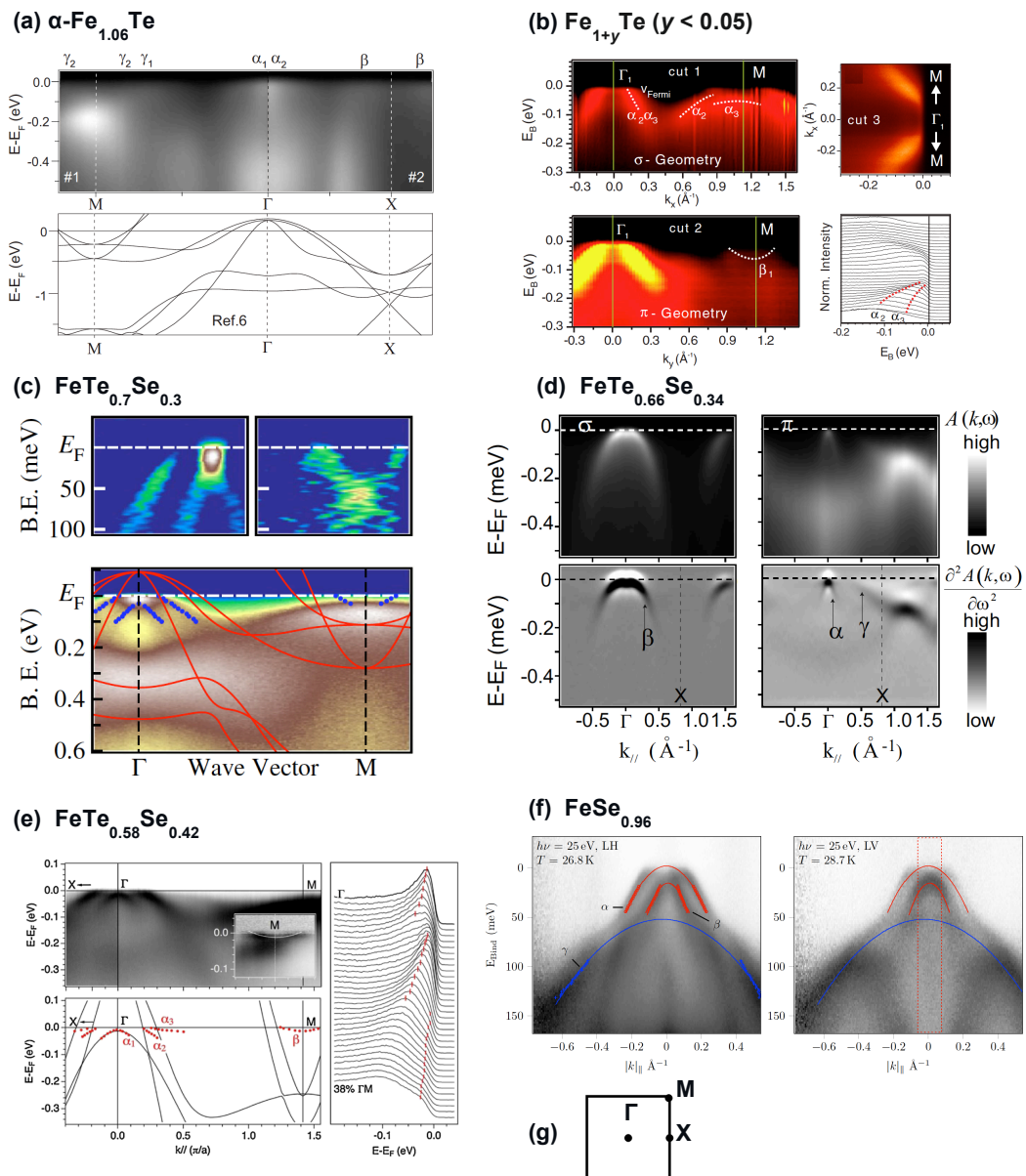
Figure 2.5: ARPES results for the $Fe_{1+y}Te_{1-x}Se_x$ for various Se concentration, x. $x = 0$ (α-$Fe_{1.06}Te$) (a) [25], $x = 0$ ($Fe_{1+y}Te$, $y < 0.05$) (b) [26], $x = 0.30$ (c) [27], $x = 0.34$ (d) [28], $x = 0.42$ (e) [24] and $x = 0.96$ ($FeSe_{0.96}$) (f) [29]. (g) Schematic diagram of the Brillouin zone. Reprinted with permission from Refs. [26] and [24, 25, 27, 28]. © (2009) and (2010), respectively, by the American Physical Society.

Fe	Te	Se	m^*/m_{band}				References
			d_{xy}	d_{yz}	d_{xz}	all bands	
1.06	1.0	0				3	Y. Zhang *et al.* [25]
< 1.05	1.0	0				2	Y. Xia *et al.* [26]
1.0	0.7	0.3				2	K. Nakayama *et al.* [27]
1.0	0.66	0.34				3	F. Chen *et al.* [28]
1.0	0.58	0.42	1	17	6		A. Tamai *et al.* [24]
1.0	0	0.96	9	3.7	3		J. Maletz *et al.* [29]

Table 2.1: Mass renormalization values obtained from ARPES data for various compositions of $Fe_{1+y}Te_{1-x}Se_x$.

Chapter 3

Principle of photoemission spectroscopy and experimental procedure

Photoemission spectroscopy (PES) is an experimental technique with long history still in extensive use. PES experiments are performed to detect the energy distribution of electrons that are excited by absorption of photons from a monochromatized light source. In the three-step model, PES can be classified into the following three independent processes [30, 31].

1. Optical excitation of the electron in the bulk.
2. Travel of the excited electron to the surface.
3. Escape of the photoelectron into the vacuum where it is detected.

3.1 General description

Photoemission spectroscopy (PES) is one of the most powerful tools to investigate the electronic structure of solids. The schematic diagram of the principle of PES is shown in Fig. 3.1. When an electron in the solid absorbs a photon of sufficiently high energy $h\nu$, it will be ejected from the solid and is emitted as a photoelectron.

From the conservation of energy, the kinetic energy $E_{\text{kin}}^{\text{vac}}$ is written as

$$E_{\text{kin}}^{\text{vac}} = h\nu - \Phi - E_{\text{B}} \tag{3.1}$$

where $E_{\text{kin}}^{\text{vac}}$ is measured from the vacuum level (E^{vac}), Φ is the work function of the sample, and E_{B} is the binding energy measured from the Fermi level (E_{F}) and/or chemical potential (μ). In real experiment, the kinetic energy

$(E_{\text{kin}} = E_{\text{kin}}^{\text{vac}} + \Phi)$ measured from E_{F} rather than $E_{\text{kin}}^{\text{vac}}$ is directly observed. Then, it is convenient to use

$$E_{\text{kin}} = h\nu - E_{\text{B}} \tag{3.2}$$

In the one-electron approximation, the binding energy is equal to the negative Hartree-Fock orbital energy,

$$E_{\text{B}} = -\epsilon_k, \tag{3.3}$$

which is sometimes called *Koopmans' binding energy*. This assumption is valid when the wave functions of both the initial and final states can be expressed by single Slater determinants of the N- and $(N-1)$-electron systems, respectively, and the one-electron wave function do not change by the removal of the electron. If one applies this approximation, the photoemission spectrum $I(E_{\text{B}})$ can be expressed as

$$I(E_{\text{B}}) \propto (E_{\text{B}} + \epsilon_k) \propto N(-E_{\text{B}}) \tag{3.4}$$

Thus, when the one-electron approximation is valid, the photoemission spectrum is proportional to the density of the occupied one-electron states $N(E)$.
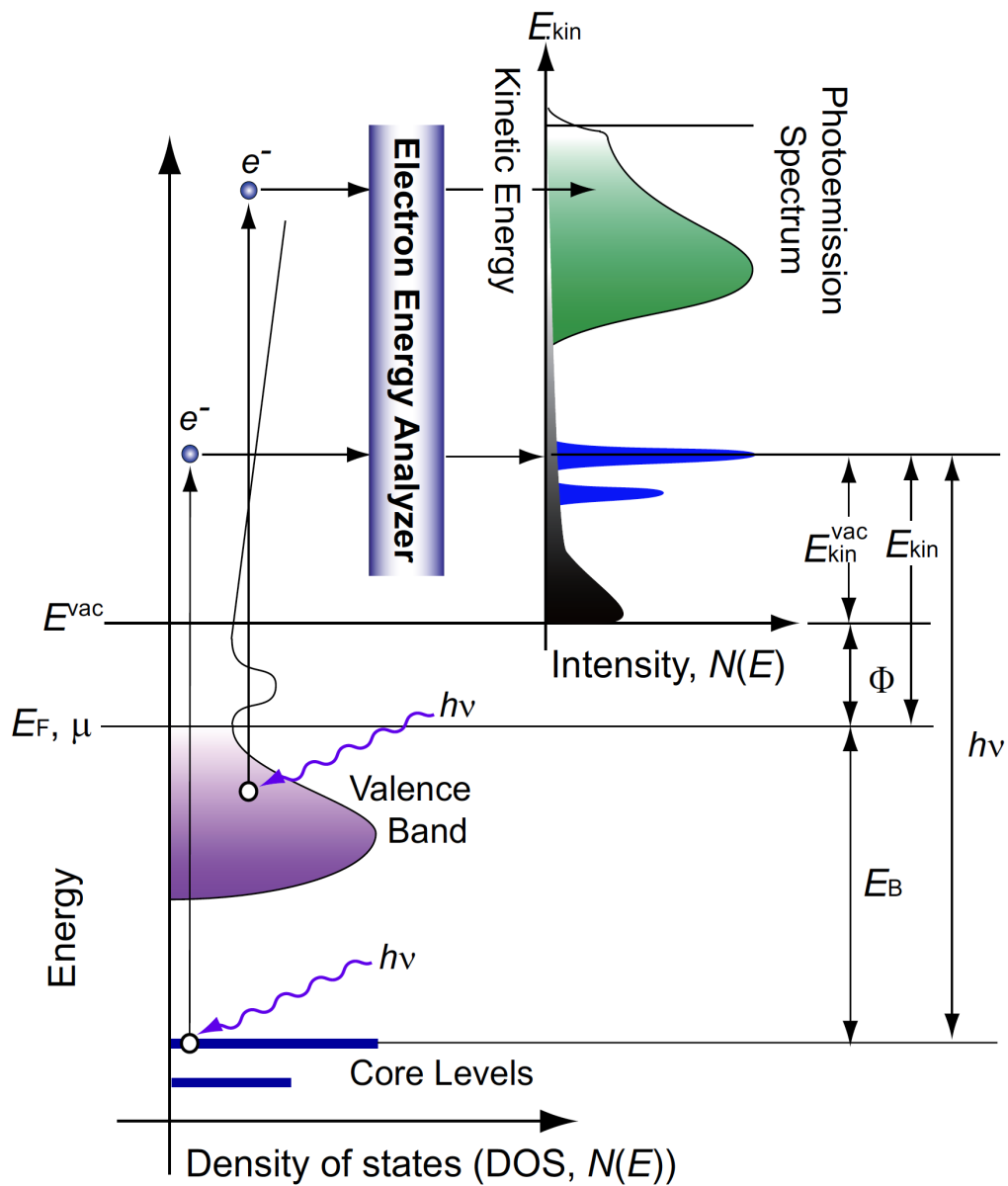
Figure 3.1: Energetics of the photoemission process (courtesy of S. Ideta). This shows the relation between the energy levels in a solid and the electron energy distribution produced by photons of energy $h\nu$.

3.2 Angle-resolved photoemission spectroscopy

Angle-resolved photoemission spectroscopy (ARPES) is the only experimental technique to determine the entire band structure of a material. ARPES can probe not only the energies but also the momenta of electrons in the solids. In the photoexcitation by low-energy photons, the momentum of the incident photon $h\nu/c$ can be neglected compared to the size of the Brillouin zone, and the wave number of the electron is conserved before and after the photoexcitation except for the reciprocal lattice vector. Therefore, the following relationship is satisfied between the wave vector of the initial state $(\boldsymbol{K}_i)$ and that of the final one $(\boldsymbol{K}_f)$:

$$\boldsymbol{K}_f = \boldsymbol{K}_i + \boldsymbol{G}, \tag{3.5}$$

where $\boldsymbol{G} = (2n_x \pi/a,\ 2n_y \pi/a,\ 2n_z \pi/a)$ where a is the reciprocal lattice vector, and n_x, n_y, and n_z are integers.

The schematic diagram of the emission of an electron from a solid to vacuum through the sample surface is shown in Fig. 3.2. When the electron is ejected from the material, the wave vector perpendicular to the surface, $(\boldsymbol{K}_{f\perp})$, is modified by the potential barrier called the inner potential (V_0), while the wave vector parallel to the surface $(\boldsymbol{K}_{f\parallel})$ is conserved. The schematic image of escape condition for the photoelectron is also shown in Fig 3.2. Therefore, the following relationship is satisfied between the wave vector parallel to the surface of the emitted electron, $\boldsymbol{k}_{f\parallel}$, and $\boldsymbol{K}_{i\parallel}$,

$$\boldsymbol{k}_{f\parallel} = \boldsymbol{p}_{f\parallel}/\hbar = \boldsymbol{K}_{f\parallel} = \boldsymbol{K}_{i\parallel}. \tag{3.6}$$
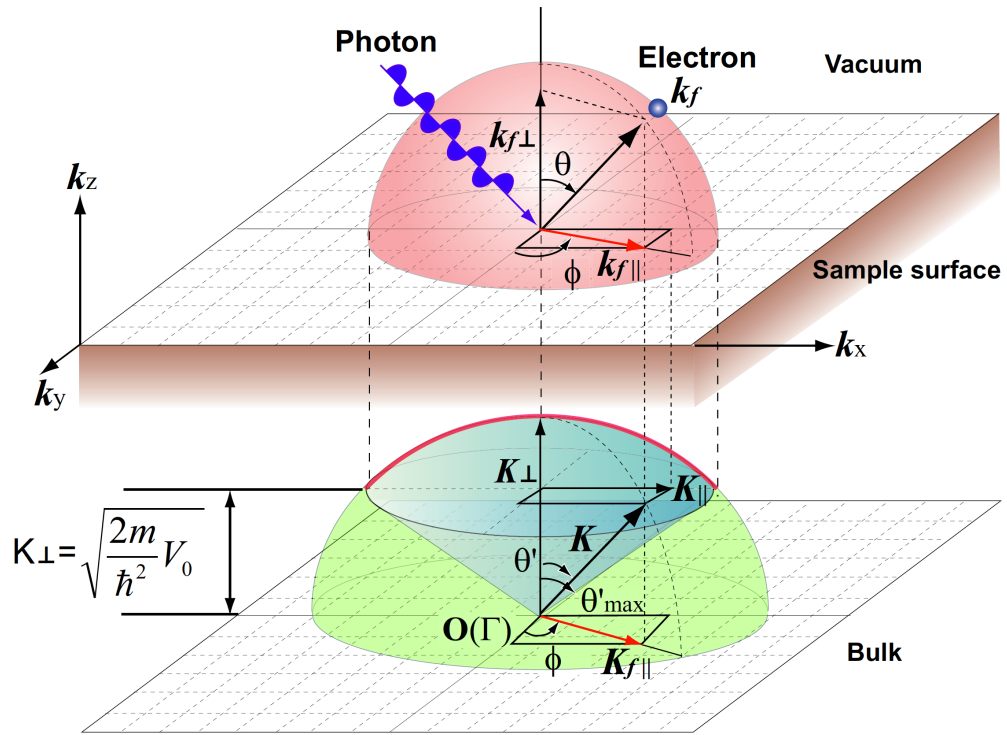
Figure 3.2: Schematic diagram of the emission of an electron from a solid to vacuum through the atomically flat single-crystal surface (courtesy of S. Ideta). The red and blue hemispheres show the external and internal escape cones for the photoelectron, respectively.

Since $\boldsymbol{p}_{f\parallel} = (p_x, p_y)$ and $\boldsymbol{p}_{f\perp} = p_z$ are related to the polar emission angle (θ, ϕ) and the photoelectron kinetic energy E_{kin}, taking into account the inner potential V_0, through the following relations

$$
\begin{aligned}
p_x &= \sqrt{2m_e E_{\text{kin}}}\, \cos\phi \sin\theta \\
&= \sqrt{2m_e(h\nu - \Phi - E_B)}\, \cos\phi \sin\theta \quad\quad (3.7) \\
p_y &= \sqrt{2m_e E_{\text{kin}}}\, \sin\phi \sin\theta \\
&= \sqrt{2m_e(h\nu - \Phi - E_B)}\, \sin\phi \sin\theta \quad\quad (3.8)
\end{aligned}
$$

$$p_z = \sqrt{2m_e(E_{\text{kin}}\cos^2\theta + V_0)}$$

$$= \sqrt{2m_e[(h\nu - \Phi - E_B)\cos^2\theta + V_0]} \qquad (3.9)$$

where m_e is the free electron mass, we can directly observe both the energy $E \equiv -E_B$ and the momentum $\boldsymbol{k} = (k_x, k_y, k_z)$ of the hole produced in the sample by the photoemission process as

$$k_x = \frac{1}{\hbar}\sqrt{2m_e(h\nu - \Phi - E_B)}\cos\phi\sin\theta + \frac{2n'_x\pi}{a} \qquad (3.10)$$

$$k_y = \frac{1}{\hbar}\sqrt{2m_e(h\nu - \Phi - E_B)}\sin\phi\sin\theta + \frac{2n'_y\pi}{b}, \qquad (3.11)$$

$$k_z = \frac{1}{\hbar}\sqrt{2m_e[(h\nu - \Phi - E_B)\cos^2\theta + V_0]} + \frac{2n'_z\pi}{c}, \qquad (3.12)$$

where n'_x, n'_y and n'_z are integers.

Figure 3.3(a) illustrates the schematic procedure for the band mapping by ARPES. If the material under study is a two-dimensional system such as the high-T_c cuprates, E and $\boldsymbol{k}_\| = (k_x, k_y)$ yield enough information to map the energy-momentum dispersion of the band structure. Then, with ARPES, we can get the two-dimensional raw data shown in the bottom panel and the energy distribution curves (EDCs) (upper panel) in Fig 3.3(b). The details of analysis are explained in the next subsection.

(a)

ARPES Spectra

Kinetic energy, E_{kin}

k_1 k_2 k_3 k_4 k_5

E_F

$E_{kin}^{vac} = -E_B + h\nu - \Phi$

$E_{kin} = h\nu - E_B$

E^{vac}

Φ

E_F

Energy

$h\nu$

$h\nu$

$h\nu$

$h\nu$

k_1 k_2 k_3 k_4 k_5 k_6

Momentum

(b)

0.2
0.1
0.0
−0.1
−0.2
−0.3
−0.4

E_F (eV)

Intensity (arb. units)

0.2
0.1
0.0
−0.1
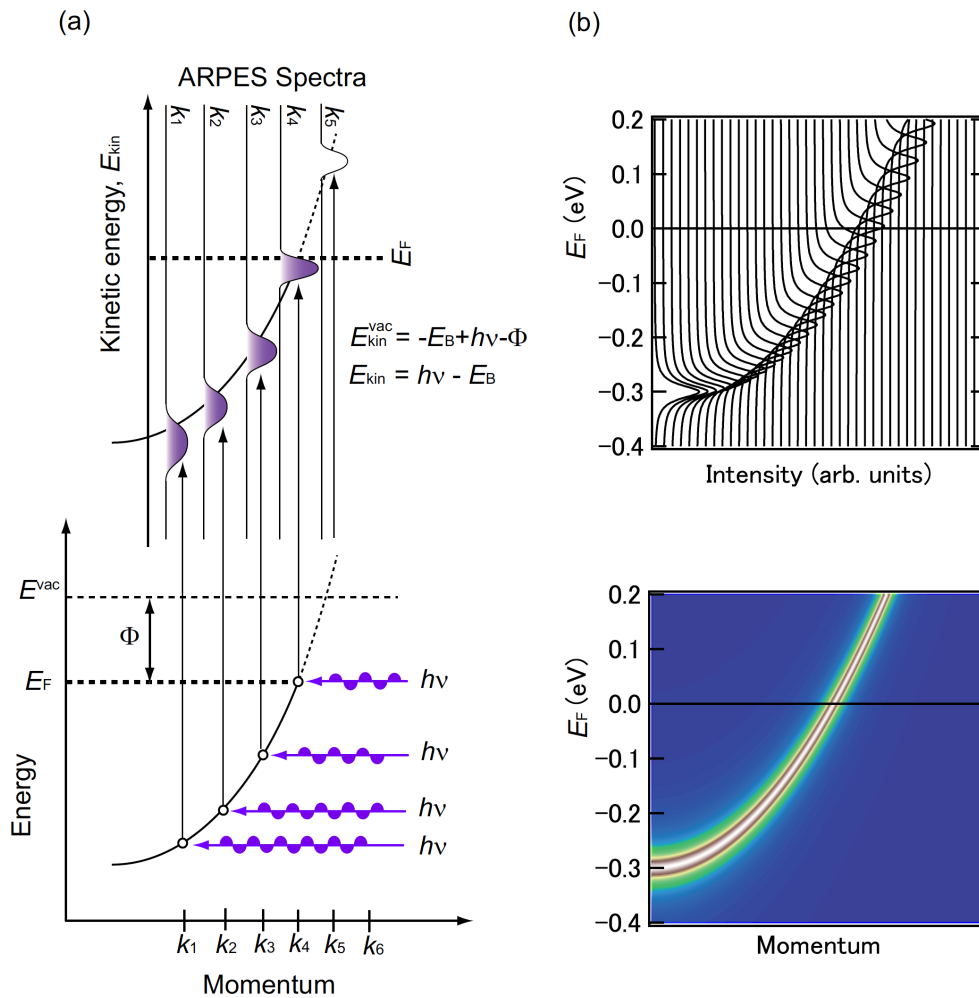−0.2
−0.3
−0.4

E_F (eV)

Momentum

Figure 3.3: Schematic diagram of the principle of angle-resolved photoemission spectroscopy (ARPES) (courtesy of S. Ideta). (a) The band dispersions in the material are directly mapped by ARPES. (b) ARPES intensity map (bottom panel) and energy distribution curves (upper panel). In ARPES experiment, we can obtain two-dimensional data of the band dispersion.

3.3 Single-particle spectral function and self-energy

Beyond the one-electron approximation, one takes many-body effects into account. In this more generalized description, photoemission process is regarded as the removal of an electron from the ground state $|\Psi_g^N\rangle$ of the N-electron system with the energy E_g^N, leaving the system in an excited state $|\Psi_n^{N-1}\rangle$ of the $(N-1)$-electron system with the energy E_n^{N-1}. Then, E_B gives the difference between E_g^N and E_n^{N-1}, namely,

$$E_B = E_n^{N-1} - E_g^N + \mu \qquad (3.13)$$

Using Fermi's golden rule, the intensity of photoemission spectrum $I(k, \omega)$, which now corresponds to the single-particle excitation spectrum of the system, is expressed as

$$I(k, \omega) \propto \sum_n \left|\langle\Psi_n^{N-1}|c_{\mathbf{k}}|\Psi_g^N\rangle\right|^2 \delta\left(\omega - E_n^{N-1} - E_g^N\right), \qquad (3.14)$$

where $c_{\mathbf{k}}$ is the annihilation operator of an electron with the momentum k and $\omega = E_{\text{kin}} - h\nu = -E_B + \mu\,(\leq \mu)$. In terms of the Green's function formalism, Eq. (3.12) can be rewritten in another expression. Let the Green's function $G(\mathbf{k})$ be defined as

$$G(\mathbf{k}, t) = -\frac{i}{\hbar}\theta(t)\langle\Psi_g^N|\{c_{\mathbf{k}}(t), c_{\mathbf{k}}^\dagger\}|\Psi_g^N\rangle, \qquad (3.15)$$

where $c_{\mathbf{k}}^\dagger$ denotes the creation operator of an electron with the momentum k, θ represents the Heaviside step function, $\{A, B\} = AB + BA$, and $A(t) \equiv e^{iHt/\hbar}Ae^{iHt/\hbar}$. From the completeness of the eigenfunctions

$$\sum_n |\Psi_n^{N-1}\rangle\langle\Psi_n^{N-1}| = 1$$

and

$$\sum_n |\Psi_n^{N+1}\rangle\langle\Psi_n^{N+1}| = 1,$$

we obtain

$$G(\mathbf{k}, \mathrm{t}) = -\frac{i}{\hbar}\theta(t)\sum_n \langle\Psi_g^N|c_\mathbf{k}(t)|\Psi_n^{N+1}\rangle\langle\Psi_n^{N+1}|c_\mathbf{k}^\dagger|\Psi_g^N\rangle$$

$$-\frac{i}{\hbar}\theta(t)\sum_n \langle\Psi_g^N|c_\mathbf{k}^\dagger|\Psi_n^{N-1}\rangle\langle\Psi_n^{N-1}|c_\mathbf{k}(t)|\Psi_g^N\rangle$$

$$= -\frac{i}{\hbar}\theta(t)\sum_n \langle\Psi_g^N|e^{iHt/\hbar}c_\mathbf{k}e^{-iHt/\hbar}|\Psi_n^{N+1}\rangle\langle\Psi_n^{N+1}|c_\mathbf{k}^\dagger|\Psi_g^N\rangle$$

$$-\frac{i}{\hbar}\theta(t)\sum_n \langle\Psi_g^N|c_\mathbf{k}^\dagger|\Psi_n^{N-1}\rangle\langle\Psi_n^{N-1}|e^{iHt/\hbar}c_\mathbf{k}e^{-iHt/\hbar}|\Psi_g^N\rangle$$

$$= -\frac{i}{\hbar}\theta(t)\sum_n |\langle\Psi_g^{N+1}|c_\mathbf{k}^\dagger|\Psi_n^N\rangle|^2 e^{iE_g^N t/\hbar}e^{-iE_n^{N+1}t/\hbar}$$

$$-\frac{i}{\hbar}\theta(t)\sum_n |\langle\Psi_g^{N-1}|c_\mathbf{k}^\dagger|\Psi_n^N\rangle|^2 e^{iE_n^{N-1}t/\hbar}e^{-iE_g^N t/\hbar} \quad (3.16)$$

where H is the Hamiltonian of the system. By Fourier-transforming Eq. (3.16) with respect to t, we have the Green's function $G(\mathbf{k}, \varepsilon)$,

$$G(\mathbf{k}, \varepsilon) = -\frac{i}{\hbar}\int_0^\infty dt\langle\Psi_g^N|\{c_\mathbf{k}(t), c_\mathbf{k}^\dagger\}|\Psi_g^N\rangle e^{i(\varepsilon+i0^+)t/\hbar}$$

$$= -\frac{i}{\hbar}\sum_n |\langle\Psi_n^{N+1}|c_\mathbf{k}^\dagger|\Psi_g^N\rangle|^2 \int_0^\infty dt e^{iE_g^N t/\hbar}e^{-iE_n^{N+1}t/\hbar}e^{i(\varepsilon+i0^+)t/\hbar}$$

$$-\frac{i}{\hbar}\sum_n |\langle\Psi_n^{N-1}|c_\mathbf{k}|\Psi_g^N\rangle|^2 \int_0^\infty dt e^{iE_n^{N-1}t/\hbar}e^{-iE_g^N t/\hbar}e^{i(\varepsilon+i0^+)t/\hbar}$$

$$= \sum_n \frac{|\langle\Psi_n^{N+1}|c_\mathbf{k}^\dagger|\Psi_g^N\rangle|^2}{\varepsilon + i0^+ - E_n^{N+1} + E_g^N} + \sum_n \frac{|\langle\Psi_n^{N-1}|c_\mathbf{k}|\Psi_g^N\rangle|^2}{\varepsilon + i0^+ + E_n^{N-1} - E_g^N}$$

$$
= \sum_n \left| \langle \Psi_n^{N+1} | c_{\mathbf{k}}^\dagger | \Psi_g^N \rangle \right|^2 \left\{ \frac{\mathcal{P}}{\varepsilon - E_n^{N+1} + E_g^N} - i\pi\delta\left(\varepsilon - E_n^{N+1} + E_g^N\right) \right\}
$$

$$
+ \sum_n \left| \langle \Psi_n^{N-1} | c_{\mathbf{k}} | \Psi_g^N \rangle \right|^2 \left\{ \frac{\mathcal{P}}{\varepsilon + E_n^{N-1} - E_g^N} - i\pi\delta\left(\varepsilon + E_n^{N-1} - E_g^N\right) \right\}
$$

$$
\tag{3.17}
$$

where $\mathcal{P}$ denotes the principal value of the integral and we have used the relation $1/(x \mp i0^+) = \mathcal{P}(1/x) \pm i\pi\delta(x)$. Then the single-particle spectral function $A(\mathbf{k}, \varepsilon)$ is given by the imaginary part of $G(\mathbf{k}, \varepsilon)$ as

$$
A(\mathbf{k}, \varepsilon) \equiv -\frac{1}{\pi} \mathrm{Im} G(\mathbf{k}, \varepsilon)
$$

$$
= \sum_n \left| \langle \Psi_n^{N+1} | c_k^\dagger | \Psi_g^N \rangle \right|^2 \delta(\varepsilon - E_n^{N+1} - E_g^N)
$$

$$
+ \sum_n \left| \langle \Psi_n^{N-1} | c_k | \Psi_g^N \rangle \right|^2 \delta(\varepsilon + E_n^{N-1} - E_g^N)
$$

$$
= A^{\varepsilon \geq E_{\mathrm{F}}}(\mathbf{k}, \varepsilon) + A^{\varepsilon \leq E_{\mathrm{F}}}. \tag{3.18}
$$

The first and the second term correspond to the spectral function for the (angle-resolved) inverse-photoemission spectrum (IPES) and the (angle-resolved) photoemission spectrum (PES), respectively. According to Eqs. (3.14) and (3.18), the formula often used in photoemission spectroscopy is finally obtained:

$$
I(\varepsilon) \propto -\frac{1}{\pi} \sum_n \mathrm{Im} G(\mathbf{k}, \varepsilon). \tag{3.19}
$$

The single-particle Green's function $G(\mathbf{k}, \varepsilon)$ can be expressed by the self-energy $\Sigma(\mathbf{k}, \varepsilon)$ which renormalizes all the interaction between particles,

$$
G(\mathbf{k}, \varepsilon) \equiv \frac{1}{\varepsilon - \varepsilon_k - \Sigma(\mathbf{k}, \varepsilon)}, \tag{3.20}
$$

where $\varepsilon_{\mathbf{k}}$ is the bare-particle energy with the momentum $\mathbf{k}$. This equation is called as Dyson's equation. In a non-interacting electron or hole system, since $\Sigma(\mathbf{k}, \varepsilon) \equiv 0$, the single-particle spectral function is written as

$$A(\mathbf{k}, \varepsilon) \equiv -\frac{1}{\pi} \mathrm{Im} G(\mathbf{k}, \varepsilon) = \delta(\varepsilon - \varepsilon_{\mathbf{k}}) \tag{3.21}$$

as shown in Fig. 3.4(b), which is *Koopmans' theorem* itself.

In an interacting system, $\Sigma(\mathbf{k}, \varepsilon)$ is not equal to zero and the photoemission spectral function is written as

$$
\begin{aligned}
A(\mathbf{k}, \varepsilon) &\equiv -\frac{1}{\pi} \mathrm{Im} G(\mathbf{k}, \varepsilon) \\
&= -\frac{1}{\pi} \frac{\mathrm{Im}\Sigma(\mathbf{k}, \varepsilon)}{\left(\varepsilon - \varepsilon_{\mathbf{k}} - \mathrm{Re}\Sigma(\mathbf{k}, \varepsilon)\right)^2 + \left(\mathrm{Im}\Sigma(\mathbf{k}, \varepsilon)\right)^2}.
\end{aligned} \tag{3.22}
$$

Figure. 3.5(a) is the schematic image of the interacting and non-interacting band dispersions. When the band dispersion influences on the electron-electron interaction, the energy at a momentum $\mathbf{k}$ shift and the band width becomes broad. Fig. 3.5(c) and (d) show the spectral function with the self-energy and the real part $\left(\mathrm{Re}\Sigma(\mathbf{k}, \varepsilon)\right)$ and imaginary part $\left(\mathrm{Im}\Sigma(\mathbf{k}, \varepsilon)\right)$ of the self-energy, which means that the $\mathrm{Re}\Sigma$ and $\mathrm{Im}\Sigma$ correspond to the value of energy shift and band width, respectively. Here, we assume that E_F is located at $\varepsilon = 0$. The real part of the pole of $G(\mathbf{k}, \varepsilon)$, $\varepsilon = \varepsilon_{\mathbf{k}}^*$ is determined by solving the equation

$$\varepsilon - \varepsilon_{\mathbf{k}}^* - \mathrm{Re}\Sigma(\mathbf{k}, \varepsilon) = 0, \tag{3.23}$$

and the residue of the pole $Z_{\mathbf{k}}(\varepsilon_{\mathbf{k}}^*)$ is given by

$$Z_{\mathbf{k}}(\varepsilon_{\mathbf{k}}^*) \left(1 - \left.\frac{\partial \mathrm{Re}\Sigma(\mathbf{k}, \varepsilon)}{\partial \varepsilon}\right|_{\varepsilon=\varepsilon_{\mathbf{k}}^*}\right)^{-1} < 1. \tag{3.24}$$

In the vicinity of $\varepsilon = \varepsilon_{\mathbf{k}}^*$, one can expand $\mathrm{Re}\Sigma(\mathbf{k}, \varepsilon)$ as follows,

$$\mathrm{Re}\Sigma(\mathbf{k}, \varepsilon) \simeq \mathrm{Re}\Sigma(\mathbf{k}, \varepsilon_\mathbf{k}^*) + \frac{\partial \mathrm{Re}\Sigma(\mathbf{k}, \varepsilon)}{\partial \varepsilon}\bigg|_{\varepsilon=\varepsilon_\mathbf{k}^*} (\varepsilon - \varepsilon_\mathbf{k}^*)$$

$$= \varepsilon - \varepsilon_\mathbf{k}^* - \frac{1}{Z_\mathbf{k}(\varepsilon_\mathbf{k}^*)}(\varepsilon - \varepsilon_\mathbf{k}^*). \tag{3.25}$$

Therefore, Eq. (3.22) is rewritten as

$$A(\mathbf{k}, \varepsilon) \simeq -\frac{Z_\mathbf{k}(\varepsilon_\mathbf{k}^*)}{\pi} \frac{Z_\mathbf{k}(\varepsilon_\mathbf{k}^*)\mathrm{Im}\Sigma(\mathbf{k}, \varepsilon)}{(\varepsilon - \varepsilon_\mathbf{k}^*)^2 + Z_\mathbf{k}(\varepsilon_\mathbf{k}^*)\big(\mathrm{Im}\Sigma(\mathbf{k}, \varepsilon)\big)^2} \tag{3.26}$$

where $Z_\mathbf{k}(\varepsilon_\mathbf{k}^*) < 1$. As shown in Fig. 3.4(c), the peak position of the quasiparticle, which is called coherence part, is located at $\varepsilon = \varepsilon_\mathbf{k}^*$ with spectral weight $Z_\mathbf{k}(\varepsilon_\mathbf{k}^*)$. The remaining spectral weight is distributed in the incoherent part away from E_F.

In the vicinity of E_F, $\varepsilon_\mathbf{k}$ can be written as $\varepsilon_\mathbf{k} = v_\mathbf{k}^* (k - k_\mathit{F})$, where $v_\mathbf{k}^* (\equiv |\nabla \varepsilon_\mathbf{k}^*|)$ is the renormalized Fermi velocity and $\mathbf{k}$ is taken perpendicular to the Fermi surface. Then, the momentum energy distribution curve (MDC) at the Fermi level ($\varepsilon = 0$) is given by

$$A(\mathbf{k}, 0) = -\frac{Z_\mathbf{k}(v_\mathbf{k}^*)}{\pi} \frac{Z_\mathbf{k}\mathrm{Im}\,\Sigma(\mathbf{k}, 0)/v_\mathbf{k}^*}{(k - k_\mathrm{F})^2 + (Z_\mathbf{k}\mathrm{Im}\,\Sigma(\mathbf{k}, 0)/v_\mathbf{k}^*)^2} \tag{3.27}$$

Thus, the MDC is given by a Lorenzian with a full width at half maximum (FWHM) of $\Delta k = 2|\mathrm{Im}\,\Sigma/v_\mathbf{k}^*|$, if the $\mathbf{k}$-dependence of $Z_\mathbf{k}$, $\mathrm{Im}\Sigma(\mathbf{k}, 0)$ and $v_\mathbf{k}^*$ can be neglected. Since the inverse life time of the quasiparticle is given by $1/\tau_\mathbf{k} = -2Z_\mathbf{k}\mathrm{Im}\Sigma$, $1/\Delta k$ represents the mean free path $l_\mathbf{k}$:

$$l_\mathbf{k} = v_\mathbf{k}^*\tau_\mathbf{k} = \frac{1}{\Delta k} \tag{3.28}$$

(a)

$\sim \mathbf{Im\Sigma(k, \varepsilon_k^*)}$

ε_k^*

$\mathbf{Re\Sigma(k, \varepsilon_k^*)}$

ε_k

ε

$\mathbf{k}$

(b)

$A(\mathbf{k}, \varepsilon)$

Quasiparticle peak

ε_k $E_F=0$ ε

(c)

$A(\mathbf{k}, \varepsilon)$

Quasiparticle peak (Choherent part)

Inchoherent part

ε_k^* $E_F=0$
$\equiv \varepsilon_k + \mathrm{Re}\,\Sigma(\mathbf{k}, \varepsilon)$

ε

(d)

$\varepsilon - \varepsilon_k$

$E_F=0$ ε

ε_k ε_k^*

$\mathbf{Re\Sigma(k, \varepsilon)}$
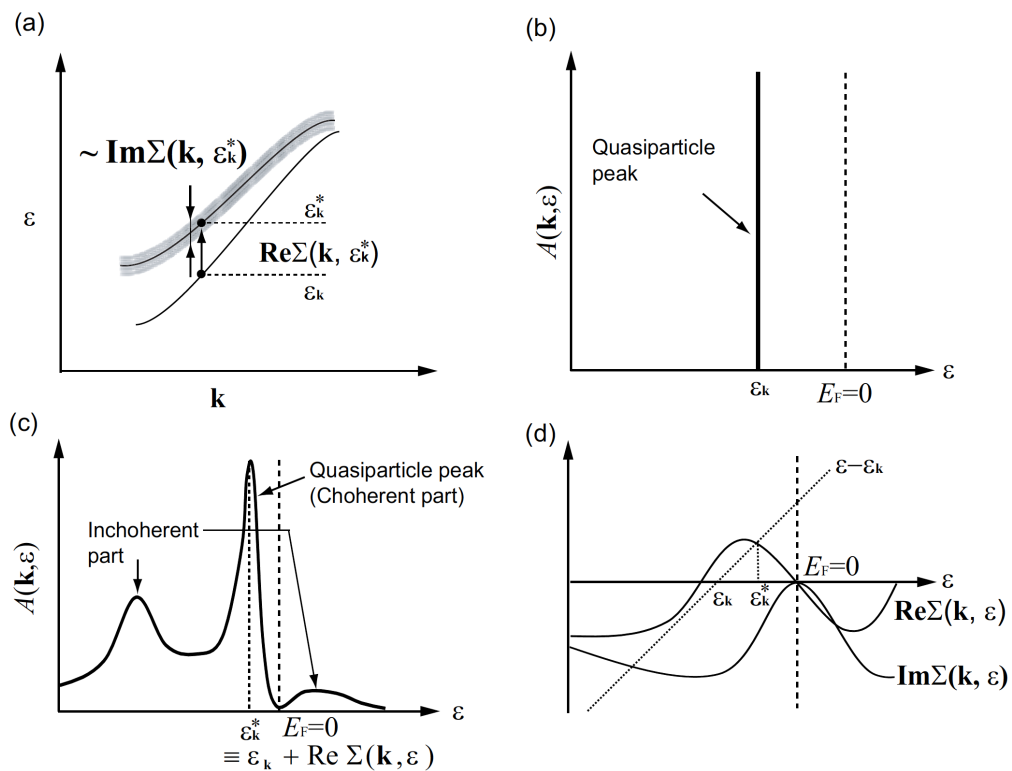
$\mathbf{Im\Sigma(k, \varepsilon)}$

Figure 3.4: Schematic diagram of the photoemission spectral function $A(\mathbf{k}, \varepsilon)$ (courtesy of S. Ideta). (a) Band dispersion affected by the electron-electron interaction deviates from the energy position of bare band by the $\mathrm{Re}\Sigma(\mathbf{k}, \varepsilon_\mathbf{k}^*)$ in the energy direction. The $\mathrm{Im}\Sigma(\mathbf{k}, \varepsilon_\mathbf{k}^*)$ denotes the band width. Spectral function $A(\mathbf{k}, \varepsilon)$ (b) when the one-electron approximation is exactly applicable and (c) when the electron correlation is taken into account. (d) The real and imaginary part of the self-energy $\Sigma(\mathbf{k}, \varepsilon)$.

The effective mass m^* on the Fermi surface is defined by

$$m^* \equiv \left(\frac{1}{\mathbf{k}}\frac{d\varepsilon_\mathbf{k}^*}{d\mathbf{k}}\bigg|_{\mathbf{k}=\mathbf{k}_\mathrm{F}}\right)^{-1}. \tag{3.29}$$

We can express $\varepsilon_\mathbf{k}^*$ in the vicinity of E_F from Eq. (3.23) as

$$\varepsilon_\mathbf{k}^* \simeq \varepsilon_\mathbf{k} + \frac{\partial \mathrm{Re}\Sigma(\mathbf{k},\varepsilon)}{\partial\varepsilon}\bigg|_{\varepsilon=0}\varepsilon_\mathbf{k}^* + \frac{\partial \mathrm{Re}\Sigma(\mathbf{k}',\varepsilon)}{\partial\mathbf{k}'}\bigg|_{\mathbf{k}'=\mathbf{k}_\mathrm{F}}(\mathbf{k}-\mathbf{k}_\mathrm{F}). \tag{3.30}$$

Then, we assume $\mathrm{Re}\Sigma(\mathbf{k}_\mathrm{F},0) \equiv 0$, because we implicitly consider the Fermi liquid. Here, when we differentiate $\mathbf{k}$ and take the limit of $\mathbf{k} = \mathbf{k}_\mathrm{F}$ in Eq. (3.30), one can obtain the following formula,

$$\frac{1}{\mathbf{k}}\frac{d\varepsilon_\mathbf{k}^*}{d\mathbf{k}}\bigg|_{\mathbf{k}=\mathbf{k}_\mathrm{F}} \simeq Z_\mathbf{k}(0)\left\{\frac{1}{\mathbf{k}}\frac{d\varepsilon_\mathbf{k}}{d\mathbf{k}}\bigg|_{\mathbf{k}=\mathbf{k}_\mathrm{F}} + \frac{\partial \mathrm{Re}\Sigma(\mathbf{k}',\varepsilon)}{\partial\mathbf{k}'}\bigg|_{\mathbf{k}'=\mathbf{k}_\mathrm{F}}\right\}. \tag{3.31}$$

When we define the band mass (m_b), ω-mass (m_ω) and $\mathbf{k}$-mass $(m_\mathbf{k})$ as

$$m_b \equiv \left(\frac{1}{\mathbf{k}}\frac{d\varepsilon_\mathbf{k}}{d\mathbf{k}}\bigg|_{\mathbf{k}=\mathbf{k}_\mathrm{F}}\right)^{-1} \tag{3.32}$$

$$\frac{m_\omega}{m_b} = \frac{1}{Z_\mathbf{k}(0)} = 1 - \frac{\partial \mathrm{Re}\Sigma(\mathbf{k},\varepsilon)}{\partial\varepsilon}\bigg|_{\varepsilon=0} \tag{3.33}$$

$$\frac{m_\mathbf{k}}{m_b} = \left(1 + \frac{m_b}{\mathbf{k}}\frac{\partial \mathrm{Re}\Sigma(\mathbf{k},\varepsilon)}{\partial\varepsilon}\bigg|_{\mathbf{k}=\mathbf{k}_\mathrm{F}}\right)^{-1}. \tag{3.34}$$

Then, the following relationship is obtained

$$\frac{m^*}{m_b} = \frac{m_\omega}{m_b}\frac{m_\mathbf{k}}{m_b}. \tag{3.35}$$

3.4 Electron escape depth

Photoemission spectroscopy is a surface sensitive experiment technique. The escape depth of photoelectrons is determined by electron-electron and electron-phonon interactions. Generally, electron-phonon scattering plays a role only at low energies below the phonon frequencies. The escape depth of the electrons λ is then determined largely by electron-electron interaction. The cross-section for electron-electron scattering σ is given by

$$\frac{d^2\sigma}{d\Omega d\varepsilon} = \frac{\hbar^2}{(\pi e a_0)} \frac{1}{q^2} \text{Im}\left\{-\frac{1}{\epsilon(q,\varepsilon)}\right\} \qquad (3.36)$$

where $\epsilon(q,\varepsilon)$ is the dielectric function, $\hbar q$ is the momentum transfer and ε is the energy transfer in the scattering process. $a_0 = 0.529$ Å, and Ω is the solid angle into which the electrons are scattered. Although $\epsilon(q,\varepsilon)$ differs from material to material, the escape depth as a function of energy roughly follows the universal curve as shown in Fig. (3.5) for all materials [32]. Then, expected for small energies (<10 eV), the electrons in solids can be approximately described by free-electron gas. In the free-electron case, the plasma frequency, which is a function of only the electron density or the mean electron-electron distance r_s, (and the damping rate of the plasmon) determined the loss function $\text{Im}\{\epsilon\}$.

The inverse escape depth λ^{-1} is then described by r_s, which is roughly equal for all materials, and one obtains

$$\lambda^{-1} \simeq \sqrt{3} \frac{a_0 R}{E_{\text{kin}}} r_s^{-3/2} \ln\left\{\left(\frac{4}{9\pi}\right)\frac{E_{\text{kin}}}{R} r_s\right\}, \qquad (3.37)$$

where $R = 13.60$ eV, and r_s is measured in units of the Bohr radius a_0. Therefore, electron-escape depth λ is given as a function of kinetic energy of electron E_{kin} as observed experimentally in Fig. (3.5), and almost all

materials show a similar energy dependence of the mean electron escape depth.
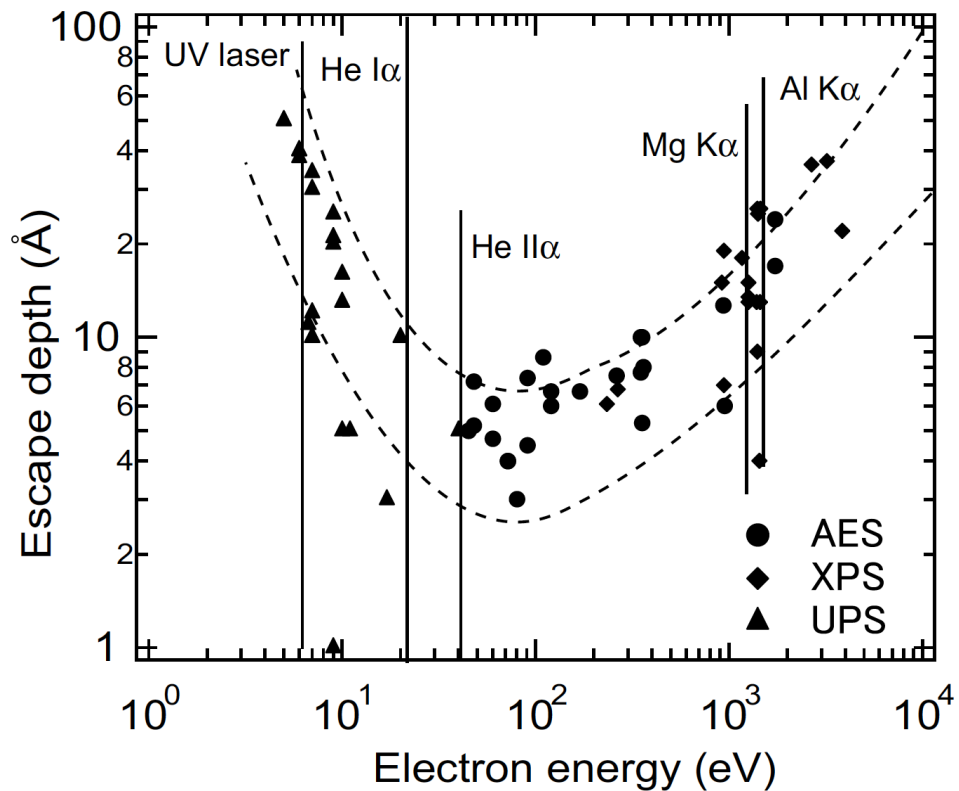

Figure 3.5: Escape depth of electrons in solids. Dashed curves indicate the approximate range of the experimental data [32]. This shows that in case of using He Iα and He IIα for UPS measurement, escape depth is ~ 15 and 10 Å, respectively. Laser source is known very bulk sensitive and the escape depth of photoelectrons is ~ 70 - 100 Å.

3.5 Resonance photoemission spectroscopy

With synchrotron radiation, one can use photons of continuously variable energy. The schematic diagram of resonance photoemission spectroscopy (RPES) is depicted in Fig. 3.6. When the energy of the incident photon is equal to the energy difference between the p core level and the valence d states, in addition to the direct photoemission of a valence d electron,

$$p^6 d^N + h\nu \longrightarrow p^6 d^{N-1} + e^-, \tag{3.38}$$

the photo-absorption and the subsequent Auger-type decay, called super Coster- Krönig decay,

$$p^6 d^N + h\nu \longrightarrow p^5 d^{N+1} \longrightarrow p^6 d^{N-1} + e^-, \tag{3.39}$$

also occurs. Since the final states of these two processes have the same electron configuration, a quantum-mechanical interference will occur. The photoemission intensity is resonantly enhanced and shows a so-called Fano profile [33], shown in Fig. 3.7. Since this enhancement takes place only for the d orbitals, one can obtain the d partial density of states in the compound.

In the $p \rightarrow d$ photoemission processes, the Fano resonance is derived from configuration interaction between the $3d$ electron emitted electronic configuration $p^6 d^{N-1}$ as a continuous state $\psi(E)$ with energy E and the core-excited electronic configuration $p^5 d^{N+1}$ as a discrete state ϕ with energy E_ϕ. These states are assumed to be orthogonal and normalized as

$$\langle \phi | \phi \rangle = 1, \langle \psi(E) | \psi(E') \rangle = \delta(E - E'), \langle \psi(E) | \phi \rangle = 0, \tag{3.40}$$

where δ denotes Dirac δ function. The matrix elements belonging to the subset of states $\psi(E)$ and ϕ are indicated by
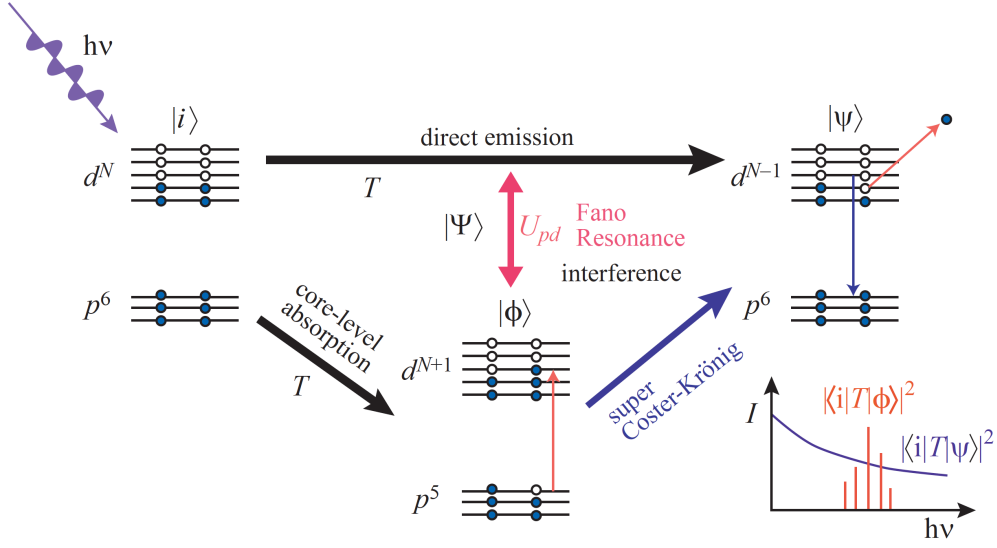
Figure 3.6: Schematic diagram of resonance photoemission spectroscopy (courtesy of W. Malaeb). Ψ and ϕ denote the continuous and discrete states, respectively. The right-down graph shows the transition probability of these states as a function of $h\nu$.

$$\langle \phi | \mathcal{H} | \phi \rangle = E_\phi, \tag{3.41}$$

$$\langle \psi(E) | \mathcal{H} | \phi \rangle = V(E), \tag{3.42}$$

$$\langle \psi(E') | \mathcal{H} | \psi(E) \rangle = E\delta(E' - E), \tag{3.43}$$

where $\mathcal{H}$ is the Hamiltonian of the system. The off-diagonal matrix element $V(E)$ is originated from the Coulomb interaction in $\mathcal{H}$, that is, $V(E) = \left\langle p^6 d^{N-1} \left| e^2 / r \right| p^5 d^{N+1} \right\rangle$, and is treated as configuration interaction between ϕ and $\Psi(E)\psi(E)$. The corresponding eigenstate has the form

$$\Psi(E) = a\phi + \int dE' b_{E'} \psi(E'). \tag{3.44}$$

The second term represents modulated $\psi(E)$ and the sum of two terms yield the phase shift Δ due to the configuration interaction between ϕ and $\psi(E)$,

which is given by

$$\Delta = -\arctan\frac{\pi|V(E)|^2}{E - E_\phi - F(E)}, \tag{3.45}$$

where

$$F(E) = \mathcal{P}\int dE' \frac{|V(E)|^2}{E - E'}. \tag{3.46}$$

The probability of excitation of the state $\Psi(E)$ is represented as the squared matrix element of the transition operator T between the initial state i ($p^6 d^N$ configuration) and the state $\Psi(E)$. The ratio of the transition probability $|\langle\Psi(E)|T|i\rangle|^2$ to the unperturbed $|\langle\psi(E)|T|i\rangle|^2$ can be represented by

$$\frac{|\langle\Psi(E)|T|i\rangle|^2}{|\langle\psi(E)|T|i\rangle|^2} = \frac{(q + \varepsilon)^2}{1 + \varepsilon^2}, \tag{3.47}$$

where

$$\varepsilon = -\cot\Delta = \frac{E - E_\phi - F(E)}{\pi|V(E)|^2}, \tag{3.48}$$

$$q = \frac{\langle\phi|T|i\rangle + \mathcal{P}\int dE'\, \langle\phi|\mathcal{H}|\psi(E')\rangle\langle\psi(E')|T|i\rangle/(E - E')}{\pi\langle\phi|\mathcal{H}|\psi(E)\rangle\langle\psi(E)|T|i\rangle}, \tag{3.49}$$

are the reduced energy variable and the parameter denotes modification of the discrete state ϕ. Figure 3.7 shows the line shapes of Eq. (3.47) for different values of q, which shows clear enhancement near $\varepsilon = 0$. Since the photoemission intensity is proportional to $|\langle\Psi(E)|T|i\rangle|^2$ when the energy of the incident photon is equal to that of the $p \rightarrow d$ excitation, one can extract the d partial density of states in the valence band by the $p \rightarrow d$ RPES.
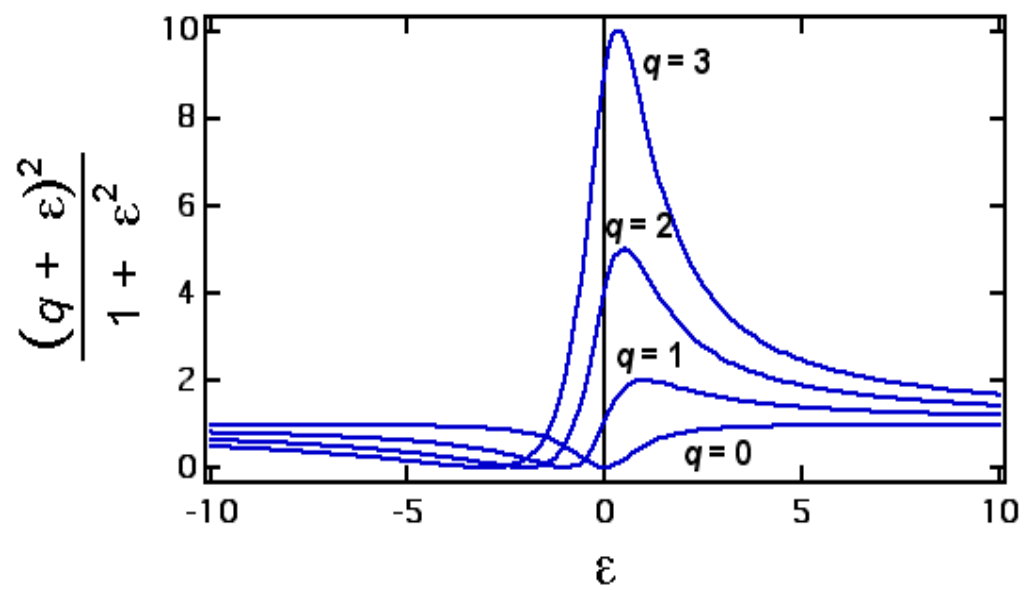
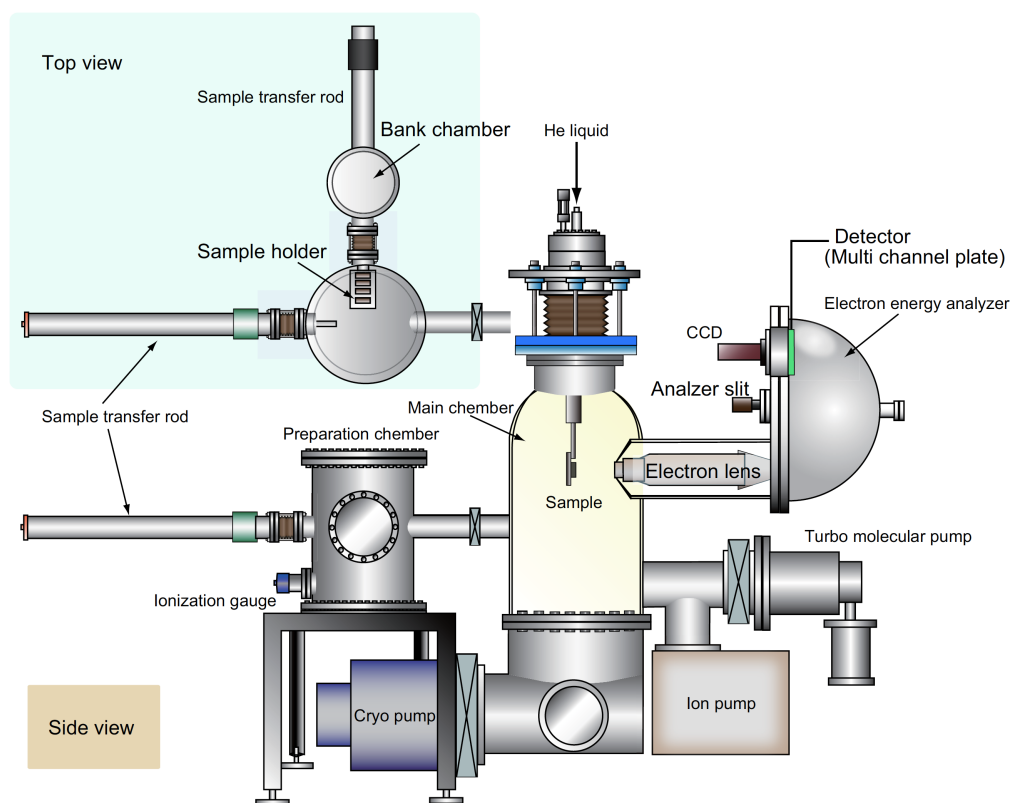Figure 3.7: Fano line shapes for different values of q.

Figure 3.8: Schematic description of the photoemission measurement system (courtesy of S. Ideta).

3.6 Experimental procedure

3.6.1 Photoemission measurement system

Basically, photoemission measurements were carried out using a hemispherical analyzer. Figure 3.8 shows a schematic description of the photoemission measurement system. Sample is introduced in the bank chamber and transferred to the preparation chamber. In the preparation chamber, we demonstrate the surface treatment to the sample, and transfer the sample to the main chamber. In the ultra-high vacuum chamber (main chamber), electrons in the solid sample are excited by incident photons and so on. The emitted photoelectrons enter the electron lens and are focused by electrostatic fields. The photoelectrons are de-accelerated by a retarding potential V_R before entering the electron analyzer. The analyzer transmits only photoelectrons with a given energy (pass energy E_P). The relationship between the retarding potential V_R and the pass energy E_P is given by

$$E_P = E_{\text{kin}} - eV_R - \varphi_A \qquad (3.50)$$

$$= \frac{eV_P}{R_2/R_1 - R_1/R_2} \qquad (3.51)$$

where φ_A is the work function of the analyzer as shown in Fig. 3.9, and V_P is applied voltage between inner and outer hemispherical analyzer. One can sweep E_{kin} by sweeping E_P or V_R. Then, the energy resolution ΔE is determined by the slit width w of inner and outer hemispheres:

$$\Delta E = \frac{wE_P}{R_1 + R_2}$$

In experiments, E_P is usually kept constant and V_R is swept so that ΔE

is kept constant independent of E_{kin}. Previously, channeltrons were widely used as an electron detector. However, to improve the detection efficiency of photoelectrons in the single-channeltron system, E_P or w must be made larger, making ΔE worse according to Eq. (3.52). To improve the detection efficiency while keeping ΔE, a multi-channel detection system with a micro-channel plate (MCP) has been used recently. SCIENTA analyzers also use an MCP as a detector. Each channel detects photoelectrons that went through different passes in the analyzer, meaning that each channel detects electrons with different pass energies. By calibrating this difference, one can improve the detection efficiency without making ΔE worse.

The resonance and angle-resolved photoemission spectroscopy (ARPES) measurements in this thesis were performed at beamline 28A at Photon Factory (PF) in KEK and beamline 5-4 at Stanford Synchrotron Radiation Laboratory (SSRL). The geometry of the beamlines and endstations will be briefly introduced in the following subsection.
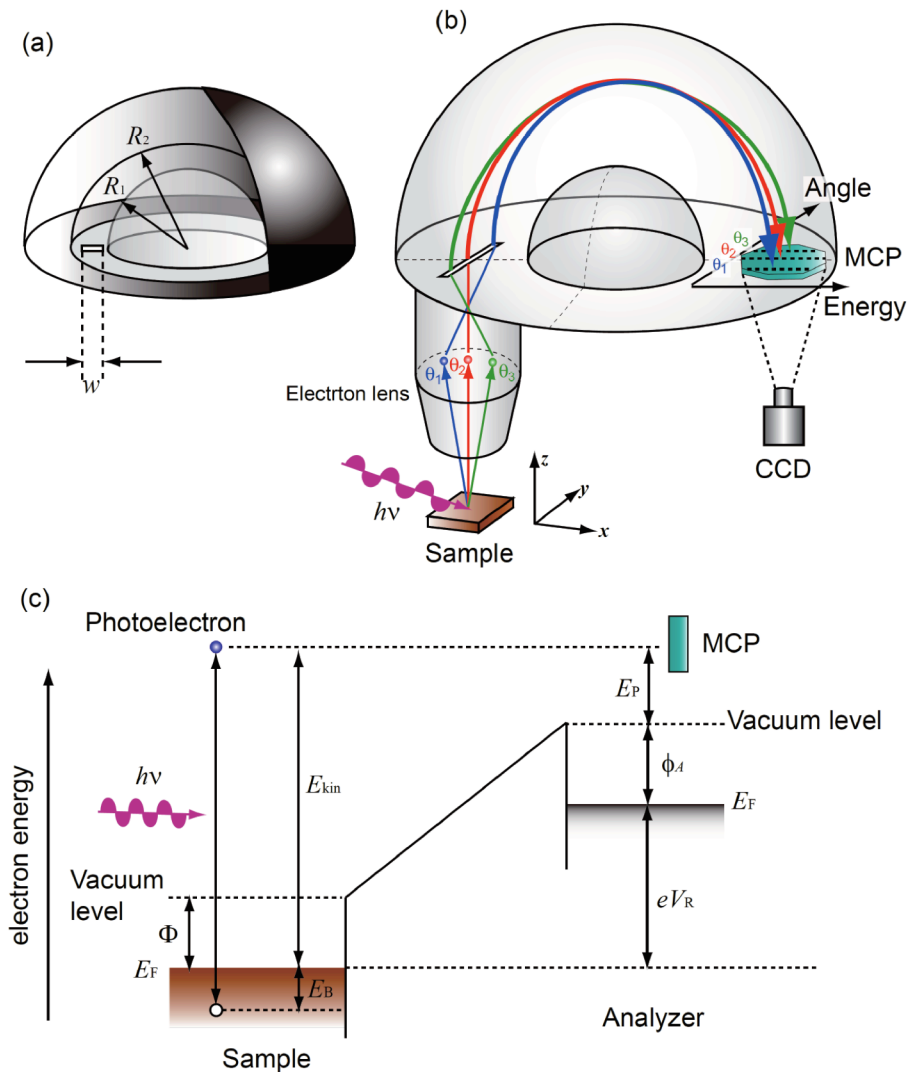
Figure 3.9: Schematic diagrams inside of the analyzer, and energy levels of the sample and analyzer (courtesy of S. Ideta). The hemispherical analyzer is constructed from the inner and outer hemispheres, where radii of hemispheres denote R_1 and R_2, respectively (a). The photoelectrons emitted from the sample are retarded by the retarding potential around the electron lens, and transit between inner and outer hemispherical analyzer (b). Diagram showing potential and energy levels for the sample and analyzer (c). Relationship between E_P and V_R can be understood from the diagram.

3.6.2 ARPES system at Photon Factory beamline 28A

The beamline 28A of Photon Factory (PF), High Energy Accelerator Research Organization (KEK) and the measurement system are described here. The beamline 28A is an undulator beamline with a Spherical Grating Monochromator (SGM) as shown in Fig. 3.10(a). It offers a wide range of photon energies from 30 to 800 eV, and both the linear and circular polarizations are available. The Endstation of the beamline is composed of a load lock chamber, a preparation chamber and the main ARPES measurement chamber as shown in Fig. 3.10(b). In the main chamber, the samples were cleaved or fractured. In the main ARPES chamber a hemispherical analyzer Gamma-data Scienta SES2002 with a two dimensional multichannel plate (MCP) detection system is attached. The manipulator in the main chamber has five degrees of freedom for sample motion: three translational and two rotational. Measurement temperature can be varied from ~9 to 300 K, and vacuum level can reach less than 10^{-10} Torr.
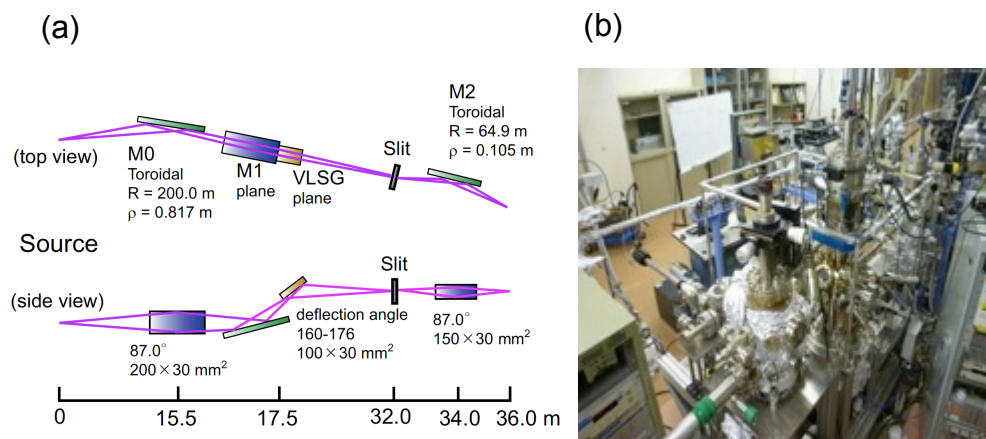

Fig 3.10: ARPES measurement system in PF BL 28A. (a) Schematic layout of the beamline. (b) ARPES measurement system.

3.6.3 ARPES system at Stanford Synchrotron Radiation Laboratory beamline 5-4

We will describe the beamline 5-4 at Stanford Synchrotron Radiation Laboratory (SSRL) and the measurent system in this section. Beamline 5-4 in an undulator beamline with a normal incidence monochromator (NIM) for photons in the vacuum ultraviolet (VUV) range light as shown in Fig. 3.11. It offers a wide range of photon energies from 15 to 32 eV. The Endstation of of the beamline is composed of a characterization chamber, an ARPES measurement chamber, preparation chamber and bank chamber. The samples were cleaved in the characterization chamber. A low energy electron diffraction (LEED) system is installed in the characterization chamber for checking the qualities and atomic structure of the sample surfaces. The cleaved sample can be easily transferred to the chamber for angle-resolved photoemission measurements. The manipulator has five degrees of freedom for sample motion. Measurement temperature can be change from ~7 to 300 K. In the ARPES chamber, a hemispherical analyzer Gamma-data Scienta R4000 is attached as shown in Fig 3.9.
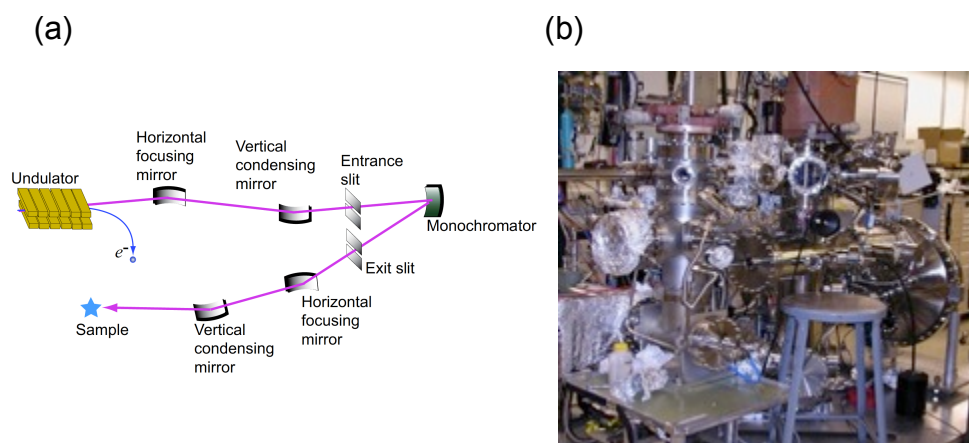
(a)   (b)

Fig 3.11: ARPES measurement system in SSRL BL 5-4. (a) Schematic layout of the beamline. (b) ARPES measurement system.

Chapter 4

Resonance photoemission study of $Fe_{1+y}Te_{1-x}Se_x$

4.1 Introduction

The discovery of the iron-based layered superconductor $La[O_{1-x}F_x]FeAs$ with a transition temperature of 26 K [4] has given renewed interest in the search for understanding the mechanism of high-T_c superconductivity. This new type of superconductors had ended the monopoly of cuprates in the high T_c superconductivity research arena. This discovery has also spurred the scientific community to synthesize new superconductors with higher T_c. The highest T_c so far, for the iron-based superconductors, was found in $Sm[O_{1-x}F_x]FeAs$ compound with a transition temperature of 55 K [34].

It is well established, that the FeAs/FeSe layers are responsible for the superconductivity in these compounds [4]. Among them, the binary 11 family of FeSe, having the simplest crystal structure, offers the possibility of providing valuable information about the origin of superconductivity in iron-based superconductors. The FeSe end member of the $FeTe_{1-x}Se_x$ compounds is superconducting and has a T_c of about 8.5 K which increases to 37 K under pressure of $\sim$ 9 GPa [35, 36]. In a study on single layer FeSe grown on $SrTiO_3$ substrate, an even higher T_c of up to 55 K has been recorded [37]. Further studies on this system found an onset of superconductivity at up to 65 K [38]. In contrast, the FeTe end member of $FeTe_{1-x}Se_x$ is not a superconductor and exhibits long range antiferromagnetic (AFM) order which is suppressed for x > 0.1 [39, 40]. For the intermediate region 0.1 < x < 0.45, a short range antiferromagnetic order appears, coexisting with superconductivity with a maximum T_c of around 14 K [41, 42].

Photoemission spectroscopy (PES) had been remarkably useful in elucidating the electronic structures and electron correlation effects in solids. In this study, we have used angle-integrated photoemission spectroscopy to investigate the valence-band spectra of the $FeTe_{1-x}Se_x$ family of iron-based superconductors.

4.2 Samples and experimental setup

$Fe_{1+y}Te_{1-x}Se_x$ (x = 0, 0.4 and 1) crystals were synthesized using the Bridgman method [43], where the Se concentration x refers to the nominal composition. A mixture of ground Fe, Te and Se powder were heated at 800 ^{o}C in an evacuated quartz tube, then slowly cooled by turning off the furnace, forming polycrystals. The obtained polycrystalline samples were heated again at 400 ^{o}C, then slowly cooled, finally obtaining single crystals, except for the polycrystalline FeSe. All the single crystals could be easily cleaved perpendicular to the c axis due to the weak van der Waals coupling that bonded the FeTe/Se layers along c axis. The nominal composition and the corresponding actual composition of the single crystals obtained from energy-dispersive x-ray analysis (EDX) are shown in Table 4.1. Although not included in the table, the FeSe samples are usually deficient in selenium ($FeSe_{1-x}$, where $x \sim 0.08$). The experiment was done at beamline 28A of Photon Factory in KEK using an SES 2002 energy analyzer. The photoemission data were taken using photons with various energies ranging from hν = 45 eV to 69 eV at a temperature of T = 20 K. We also take high temperature (T = 80 K) data, just above the Néel temperature of ~70 K for $Fe_{1.08}Te$, to cover the paramagnetic normal states of all the composition. The details of the beam line can be found in Chapter 3. All the samples were cleaved (or fractured in case of the polycrystalline $FeSe_{1-x}$) *in situ* and measured under a base pressure better than 2 x 10^{-10} Torr.

Nominal Se	Fe	Te	Se
0.4	1	0.59	0.41
0	1.08	1	0

Table 4.1: Nominal Se concentration and the actual elemental composition of $Fe_{1+y}Te_{1-x}Se_x$. The actual composition for the single crystals was obtained using energy-dispersive x-ray spectroscopy (EDX).

4.3 Results and discussion

4.3.1 Valence-band spectra

Figure 4.1 presents the valence-band spectra of $Fe_{1+y}Te_{1-x}Se_x$ ($x = 0$, 0.4, 1). Three main structures can be found in the valence band of FeSe ($x = 1$), a sharp peak near the Fermi level (E_F) and two broad structures at $\sim$-2 eV and $\sim$-4 eV, denoted as A, B and C, respectively. These structures are consistent with the previous reports on FeSe [44–46], except for the fourth structure that is located in a much higher binding energy not covered in our data. The peak structure A in FeSe splits into two distinct features in the compounds with Te content (in going from $x = 0$ to $x = 0.4$), and the separation increases with increasing Te content. Structures B and C are well separated in FeSe, but not in the case of $x = 0$ (FeTe) and $x = 0.4$, partly because feature C is broadened and shifted to lower energies. For comparison, the DFT-based band-structure calculation [23] result is displayed at the bottom of Fig. 4.1. According to the previous PES studies of FeSe and band-structure calculations [23, 47], structures A and B correspond to the Fe 3d

states and structure C reflects the hybridization of Fe $3d$ and Se $4p$ states. In addition, the calculated spectra from Yokoya *et al*. [46], shown in Fig. 4.1(c), reveal strong composition dependence of the density of states (DOS) shape in Fe $3d$ states, namely, a dominant peak with shoulder structures in FeSe and a doublet in FeTe. The composition dependence, however, shows a weaker dependence in the chalcogenides p DOS due to the shifted chalcogenides p levels. This difference reflects the change in the chalcogen height, distance between the chalcogen atom and the Fe plane as shown in Fig. 4.1(d).
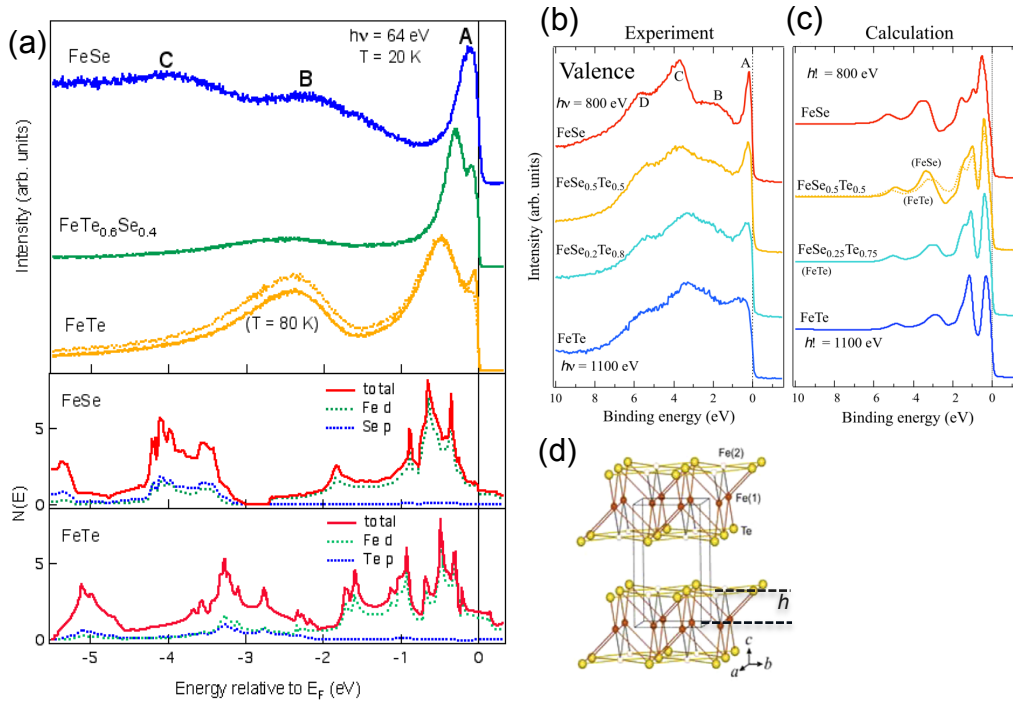
Figure 4.1: (a) Top panel: Valence-band photoemission spectra of $Fe_{1+y}Te_{1-x}Se_x$ (x = 0, 0.4, 1) measured at 20 K. DFT-based band-structure calculations for FeTe and FeSe [23] are also shown in the bottom panels. For comparison, Yokoya *et al.* [46] PES experiment is also shown in (b) with their calculation (c). (d) Crystal structure of $Fe_{1+y}Te$ showing the chalcogen height, h [14].

To further investigate the composition dependence of the spectral shape, we have carried out resonance photoemission measurements for $FeTe_{1-x}Se_x$ with different compositions ($x = 0, 0.4, 1$).

4.3.2 Resonance photoemission spectra

Figure 4.2 shows the valence-band spectra of $FeTe_{1-x}Se_x$ ($x = 0, 0.4, 1$) taken at various photon energies in the Fe $3p \to 3d$ core excitation region. These spectra have been normalized to a mirror current of the beam line and the gold absorption coefficient as a function of photon energy [48]. All of the near-E_F main features of the spectra, indicated by arrow markers, for all the compositions show strong photon energy dependence. Taking a closer look at the photoemission intensity as a function of photon energy shown in Fig. 4.3 one can see an increase in intensity from $hv \sim 53$ eV to $hv \sim 57$ eV. This indicates that the Fe $3p \to 3d$ resonance occurs at around $hv \sim 55$ eV, which confirms that the states from E_F down -2 eV are mainly Fe $3d$ states and those of the broad feature around -4 eV in FeSe represent hybridized Se $4p$ and Fe $3d$ states.
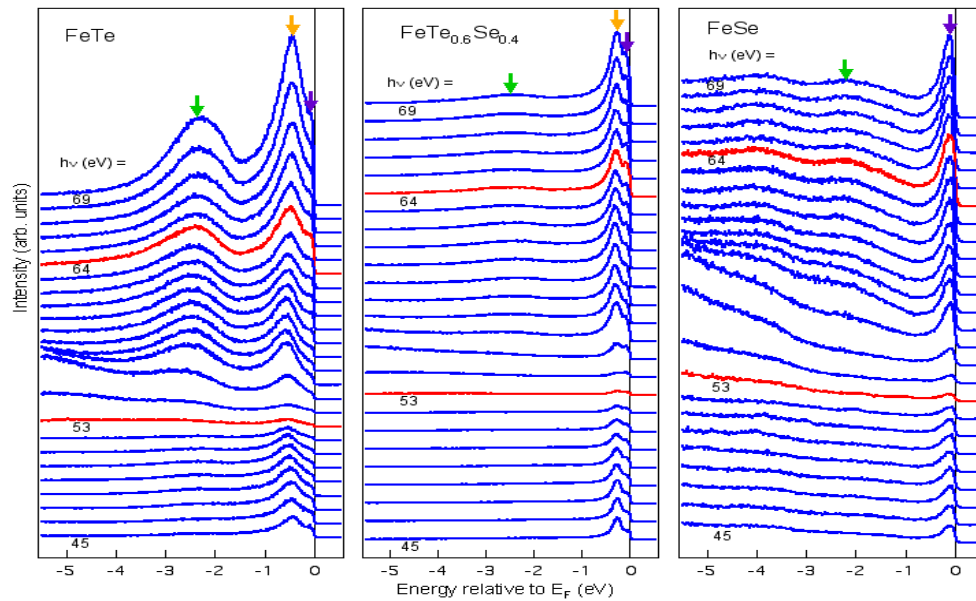
Figure 4.2: Valence-band photoemission spectra of FeTe$_{1-x}$Se$_x$ (x = 0, 0.4, 1) in the Fe $3p \rightarrow 3d$ core absorption region. Red lines highlight the on-resonance and off-resonance spectra. Vertical arrows show the position of main features in the valence-band spectra.
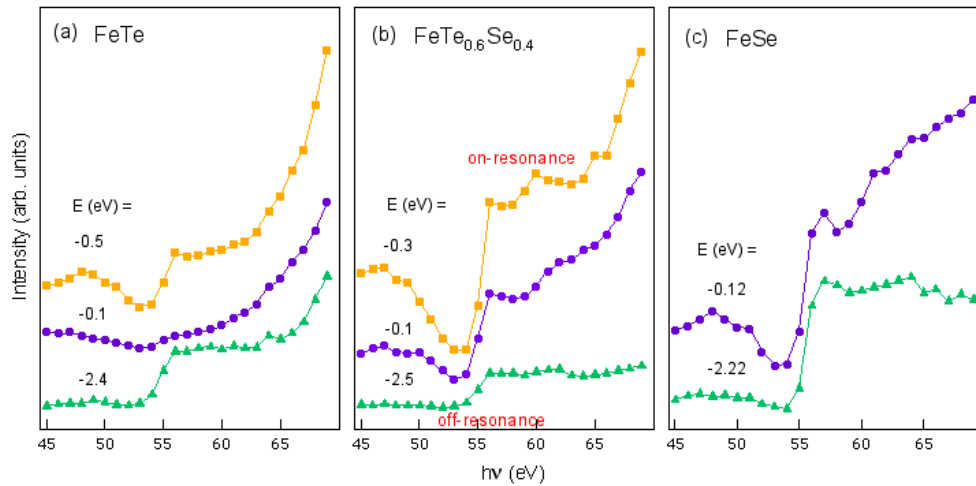

Figure 4.3: Photon-energy dependence of the photoemission intensities at binding energies corresponding to the main structures in the valence-band spectra, shown by the arrow markers in Fig. 4.2.

4.3.3 Partial density of states (PDOS)

Figure 4.4 shows the Fe $3d$ partial density of states (PDOS) of FeTe (a), $FeTe_{0.6}Se_{0.4}$ (b) and FeSe (c). The partial density of states (PDOS) for the Fe $3d$ electrons is taken from the difference between the on-resonance and off-resonance valence band spectra. As for the PDOS of FeTe, we used the high temperature 80 K data, well above the first-order magnetostructural transition temperature around 70 K. Compared with the 20 K data, the near-E_F spectral intensity is higher at 80 K where we can clearly see two distinct peak structures in the near-E_F region. The two distinct structures found in FeTe and $FeTe_{0.6}Se_{0.4}$ merge into a single peak structure in FeSe. Although the experimental data agree qualitatively well with the calculation, some discrepancies can be observed. The energy positions of the near E_F structure and the higher binding energy structures observed in experiment occur at somewhat lower and higher binding energies, respectively, than predicted by the calculation. This deviation can be explained by mass renormalization effect. The self-energy correction to the band structure calculations was proposed to yield a mass renormalization value of about 1.8 - 3.6 and also to separate an incoherent part from the spectrum [44, 45], which corresponds to the lower Hubbard band seen in LDA + DMFT studies [47].
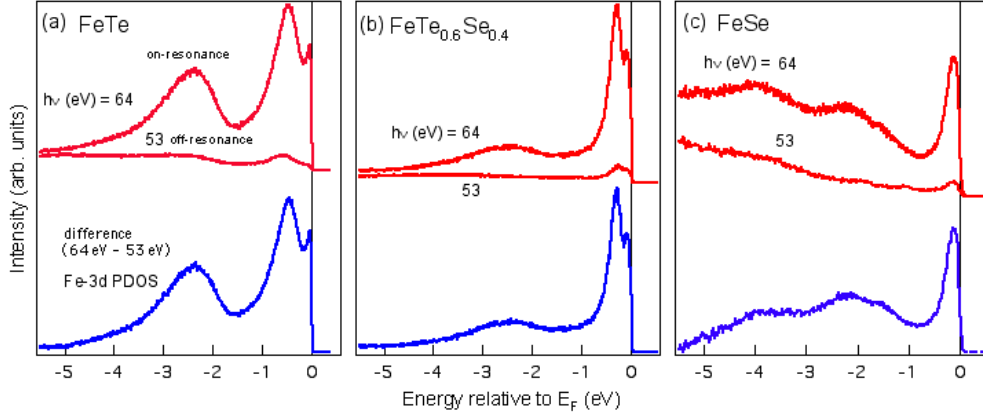
Fig. 4.4: On-resonance and off-resonance spectra of of FeTe (a), $FeTe_{0.6}Se_{0.4}$ (b), and FeSe (c) and their Fe 3d PDOS obtained by subtracting the off-resonance from the on-resonance spectra.

4.3.4 Comparison with ARPES results

Figure 4.5 shows the ARPES spectra measured along the Γ-M high-symmetry line for the $x = 0$ and $x = 0.4$ compounds. Single crystals of FeSe ($x = 1$) were not available, and hence ARPES was not possible. For the $x = 0$ and $x = 0.4$ samples, the strongest peak structure in the PDOS located at a binding energy of around $0.4 - 0.5$ eV corresponds to the flat band in the ARPES spectra intensity located around the Γ point, which comes mainly from the band dominated by d_{z^2} orbital character. The structure at E_F comes from the bands of d_{yz}, d_{xz} and d_{xy} orbital character. The shift of the strongest peak towards the Fermi level with the increase of the Se content can be explained by the shift of the d_{z^2} band towards the Fermi level. The strongest peak structure can then be attributed mainly to the d_{z^2} band. The shift of the d_{z^2} band, in effect, also reduces the splitting of the two near-E_F structures in $x = 0$ and $x = 0.4$, which finally merges in FeSe. The difference in the energy position of the d_{z^2} band is also consistent with DFT calculations [23, 26] for FeTe and FeSe wherein the d_{z^2} band is located at a higher binding energy in

the former than in the latter. Comparing the band dispersions from ARPES and calculation, one can see that the experimental bands are located at lower binding energy than the calculated ones. By adjusting the energy scale of the band calculation to match the ARPES data, the mass renormalization of the d_{z^2} band was obtained to be around 2. In order to determine the value of the correlation from the PDOS more quantitatively, careful analysis, like the phenomenological self-energy correction, is needed.
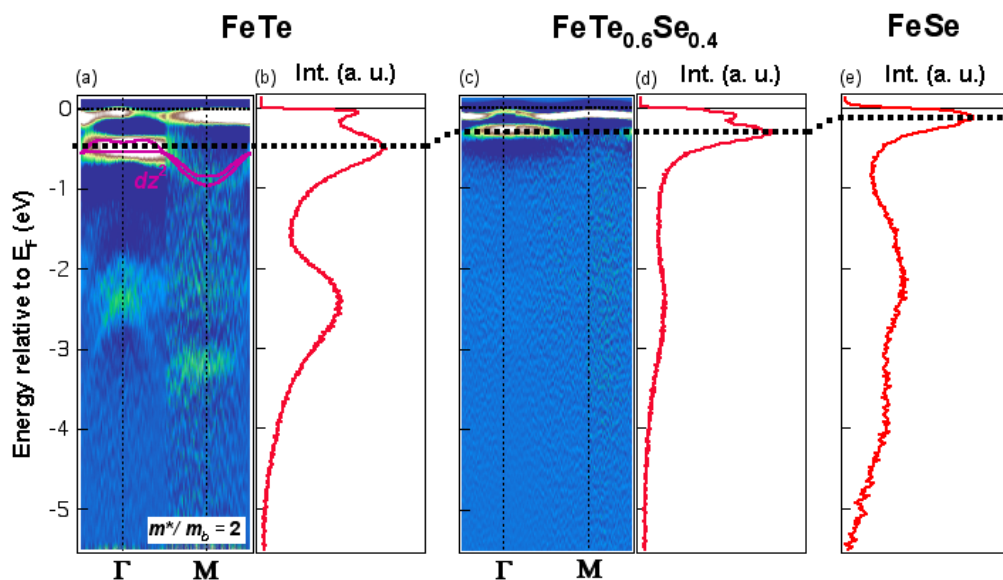

Fig. 4.5: Second derivatives of the ARPES intensity with respect to energy for FeTe (a) and FeTe$_{0.6}$Se$_{0.4}$ (c). For comparison, the PDOS of FeTe (b), FeTe$_{0.6}$Se$_{0.4}$ (d), and FeSe (e) are also plotted. The overlaid pink lines are the calculated d_{z^2} band [23, 26], rescaled to fit the ARPES spectra. Black dotted lines are guides to the eye to indicate the correspondence between the ARPES spectra and the peak in the PDOS.

4.4 Conclusion

We have performed a resonance photoemission study to investigate the composition dependence of the electronic structure of the $Fe_{1+y}Te_{1-x}Se_x$ (x = 0, 0.4, 1) compounds. Like the other iron-based superconductors, the near-E_F density of states is dominated by the Fe $3d$ states. The strongest peak structure is attributed to bands of Fe $3d_{z^2}$ orbital character, with a moderate mass renormalization factor of about 2, which is consistent with the DMFT + DFT calculation [13]. The resonance photoemission spectroscopy has difficulty in resolving the different orbital characters of the bands that composed the density of states at E_F, it is imperative to analyze angle-resolved photoemission spectra in more detail to further investigate the orbital dependent nature of the electron correlation on this type of material.

Chapter 5

Strength of electron correlation in $Fe_{1+y}Te_{1-x}Se_x$ revealed by angle-resolved photoemission spectroscopy

5.1 Introduction

The new type of high-T_c superconductors iron pnictides and chalcogenides, owing to their surprisingly high transition temperature, are subjects of extensive research aiming to understand the mechanism of high-T_c superconductivity [4]. They all share the same basic building blocks, but a significant variation have been observed in their physical properties, such as magnetic ordered moments, effective masses, superconducting gaps and transition temperature [13]. Strong electron correlation have played a vital role in the cuprates, while it is still not yet clear as to what extent this affects the superconductivity in iron pnictides and chalcogenides. Combined dynamical mean-field theory [50] and density functional theory (DMFT + DFT) studies have given the strength of electron correlation in these materials [13, 51]. In addition, the $FeTe_{1-x}Se_x$ 11 system is the simplest in terms of its crystal structures, consisting only of the FeSe/FeTe layers, without intermediate layers found in other families of iron-based superconductors [15, 52, 53]. Thus, it is of utmost importance to fully understand this simple system as this may give us valuable insight into the origin of the superconductivity in the iron-based compounds.

According to the DMFT + DFT calculation [13], the FeTe end member of $Fe_{1+y}Te_{1-x}Se_x$ is predicted to exhibit the strongest electron correlation and

strongest orbital dependence among the iron-based superconductors. FeSe, on the other hand, shows only moderate electron correlation and its orbital dependence, comparable to the other iron-based superconductor. It is also interesting to note that FeSe is a superconductor [35-37] while FeTe is not [39, 40]. In fact, the intermediate correlation strength and large degeneracy seem to be a requirement for superconductivity, while the too large orbital differentiation seems harmful as exhibited by FeTe [13, 26]. The obvious difference between the two chalcogenides, FeTe and FeSe, is their chalcogen height, the distance from the chalcogen (Te/Se) to the Fe plane. The FeTe has larger atomic radius and therefore has higher chalcogen height than in FeSe. Alloying FeTe with FeSe may give us insight into how the strength of electron correlation and its orbital dependence change with the change in the composition or the chalcogen height.

Several ARPES studies have been done on the $FeTe_{1-x}Se_x$ compounds. However, there is no general consensus yet on the systematic evolution of the electronic structure and electron correlation strength. Depending on the Se concentration, x, different and sometimes contradicting results has been obtained. For the FeTe end up to $x = 0.3$, two band dispersions were observed around the zone center Γ point, where the bands are uniformly renormalized with a factor of about 2 or 3 [24 - 26]. For $x = 0.34$, three bands were observed with a uniform mass renormalization of about 3 [25]. From $x = 0.34$ up to the FeSe end, all the three bands were observed, this time the mass renormalization exhibits strong orbital dependence [26, 27, 54, 55]. This results show that the electronic structure and electron correlation is highly dependent on the concentration of Se and Te or to the change in the chalcogen height. To shed light on this matter, we performed composition dependent ARPES studies of the electronic structure of $Fe_{1+y}Te_{1-x}Se_x$ compounds for x = 0, 0.1, 0.2, 0.4.

5.2 Samples and experimental setup

Fe$_{1+y}$Te$_{1-x}$Se$_x$ (x = 0, 0.1, 02 and 0.4) single crystals were synthesized using the same method as described in Chapter 4, the Bridgman method. The experiment was done at beamline 5-4 of SSRL using an R4000 energy analyzer. The photoemission data were taken using photons with energy of hν = 22 eV at various temperatures: T = 80 K, 40 K, 20 K and 9 K for x = 0, 0.1, 0.2 and 0.4 respectively, focusing only on the paramagnetic normal states of the compound (see Fig. 2.2 for the Se concentration-dependence phase diagram of Fe$_{1+y}$Te$_{1-x}$Se$_x$). The x = 0.4 data taken at 9 K did not show any superconducting gap and hence can be regarded as a normal state data. The details of the beam line can be found in Chapter 3. All the samples were cleaved *in situ* and measured under a base pressure better than 3 x 10^{-11} Torr.

Nominal Se	Fe	Te	Se
0.4	1	0.59	0.41
0.2	1.06	0.8	0.2
0.1	1.09	0.9	0.1
0	1.08	1	0

Table 5.1: Nominal and actual elemental composition of Fe$_{1+y}$Te$_{1-x}$Se$_x$. The actual composition was obtained using energy-dispersive x-ray spectroscopy (EDX).

5.3 Results and discussion

In Chapter 4, we were able to obtain the mass renormalization for the d_{z^2} band, which is located at the binding energy of around ~ 0.3 - 0.5eV. However, the density of states at the Fermi energy is difficult to resolve with the resonance photoemission data. To further investigate the density of states and the band dispersions at the Fermi energy, we perform high-resolution angle-resolved photoemission measurements. We shall focus our analysis only on the band dispersions around the Γ point, where the bands are easily observed due to high photoemission intensity around this point.

5.3.1 Band dispersions

Figure 5.1(a) shows the ARPES spectra measured along the Γ-M high-symmetry line for $Fe_{1.08}Te$ ($x = 0$). Even though the spectra are broad in the raw data, which is quite normal because of strong electronic correlations in this compound [25], one can still clearly see two band dispersions from the second-derivative of the ARPES spectra with respect to momentum [see Fig. 5.1(b)]. A third weak, less dispersive band is also discernable by looking closely at Fig. 5.1(c), the second-derivative plot of the intensity with respect to momentum. It looks like no band seems to cross the Fermi level. Careful analysis on the momentum distribution curves (MDCs) and energy distribution curves (EDCs) confirmed that indeed no band has crossed the Fermi energy and thereby does not contribute to the Fermi surface.

Following Chen *et al.* [28] assignment of the orbital character of the band dispersions from their $FeTe_{0.66}Se_{34}$ polarization-dependent ARPES measurements, and from band calculations [23, 56], we were able to correctly assign the orbital character to each band: The Fe 3 d_{xz}, d_{yz} and d_{xy} bands for the inner, middle and outer bands, respectively. For comparison with the LDA band calculations shown in Fig. 5.5, we have fitted the calculated band

structures to the experimental ones. However, we need to rescale the energy of the calculated band structure to match with the experimental results. This reflects the mass renormalization of the energy bands. In addition to the energy rescaling, it is also necessary to introduce additional shifts of the energy. Contrary to the previous photoemission results [24 – 28], the mass renormalization exhibits strong orbital dependence and has different values for each orbital. Before tackling the mass renormalization in detail, let me first continue to discuss the composition dependence of the band dispersion in the Se-substituted compounds.

The same procedure of analysis has been done on the other compounds. Figures 5.2, 5.3 and 5.4 show the ARPES results for the $FeTe_{0.9}Se_{0.1}$ ($x = 0.1$), $FeTe_{0.8}Se_{0.2}$ ($x = 0.2$) and $FeTe_{0.6}Se_{0.4}$ ($x = 0.4$), respectively. For the Se-substituted compounds, all the three band dispersions can be seen more clearly around the Γ point. For these compounds, the d_{xy} (outer band) and d_{yz} (middle band) orbital bands seem to cross the Fermi level. These two bands now form two hole pockets around the Γ point and thus contribute to the Fermi surface. However, the d_{xz} (inner band) is still buried in the higher binding energy than the other two, and remains no contribution to the Fermi surface.

As for the composition dependence, a trend has emerged for each of the band. The d_{xz} band shifts towards the Fermi level as Se concentration is increased while the other two bands are unaffected by the change of the composition. The reason for this behavior will be discussed in detail in the following subsection.
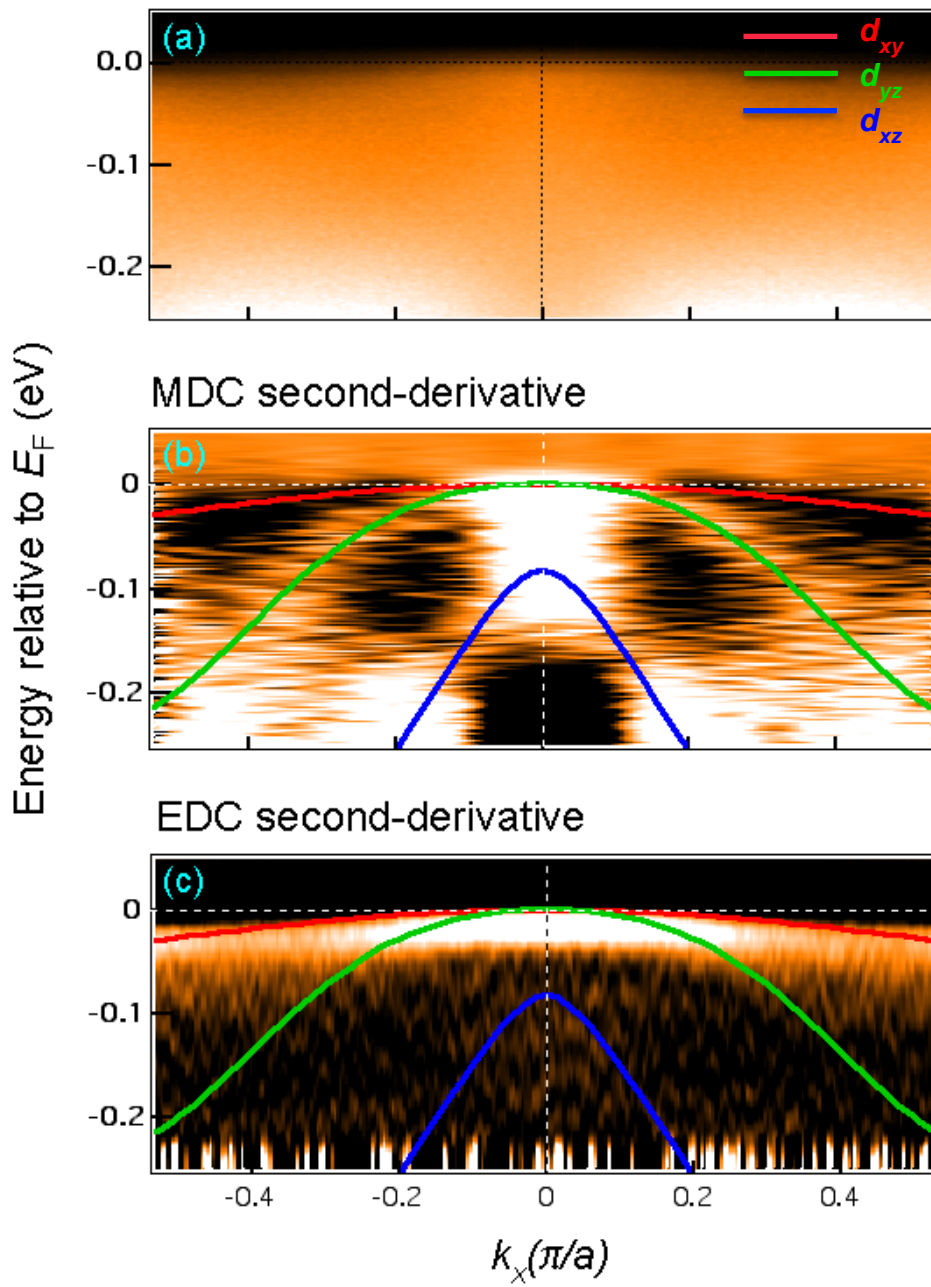
Fig. 5.1: (a) ARPES intensity plot of FeTe ($x = 0$) in the vicinity of E_F along the $\Gamma - M$ direction. (b), (c) Second-derivate plots of the ARPES spectra with respect to momentum and energy, respectively. The overlaid lines are calculated bands scaled with respect to energy to fit the experimental band dispersions.
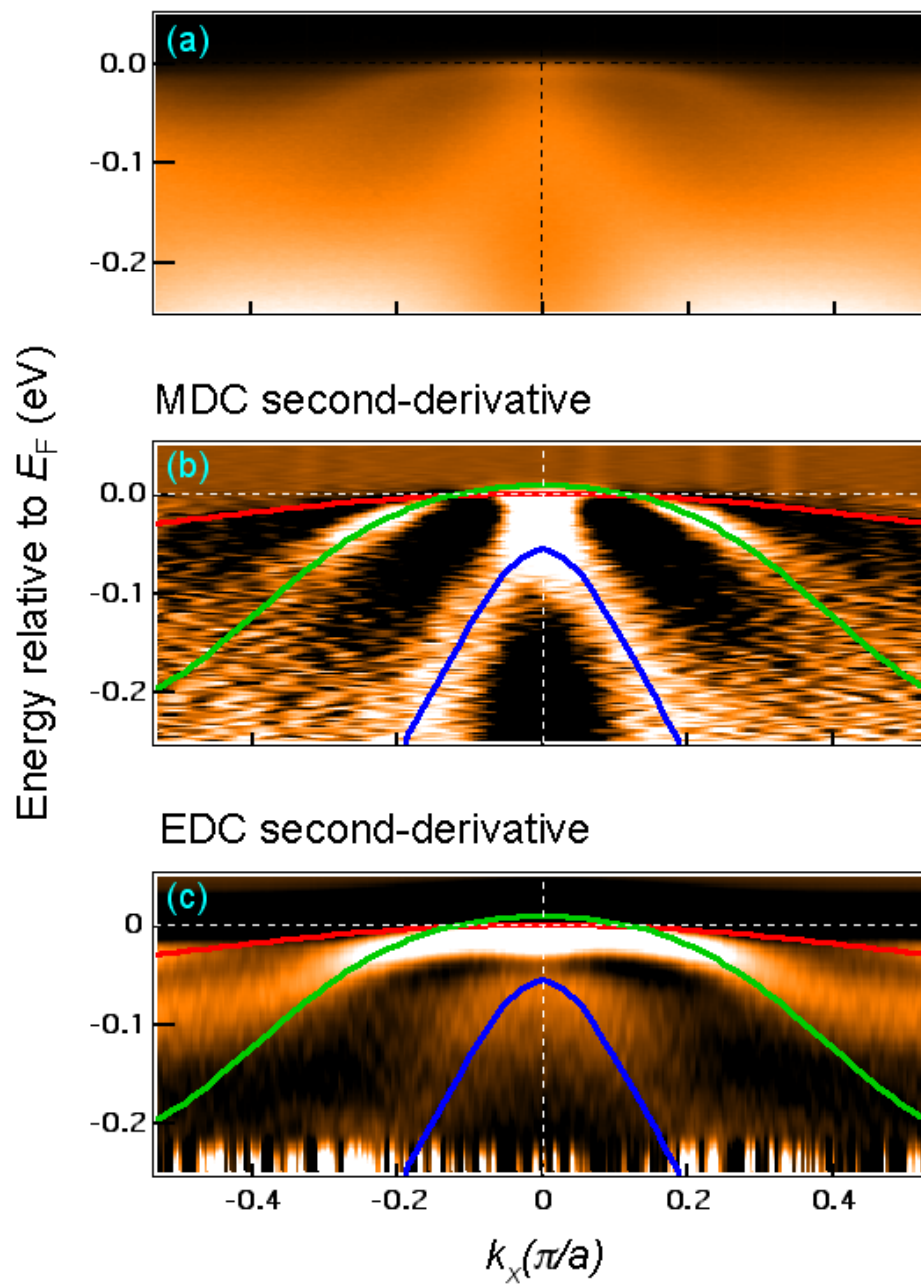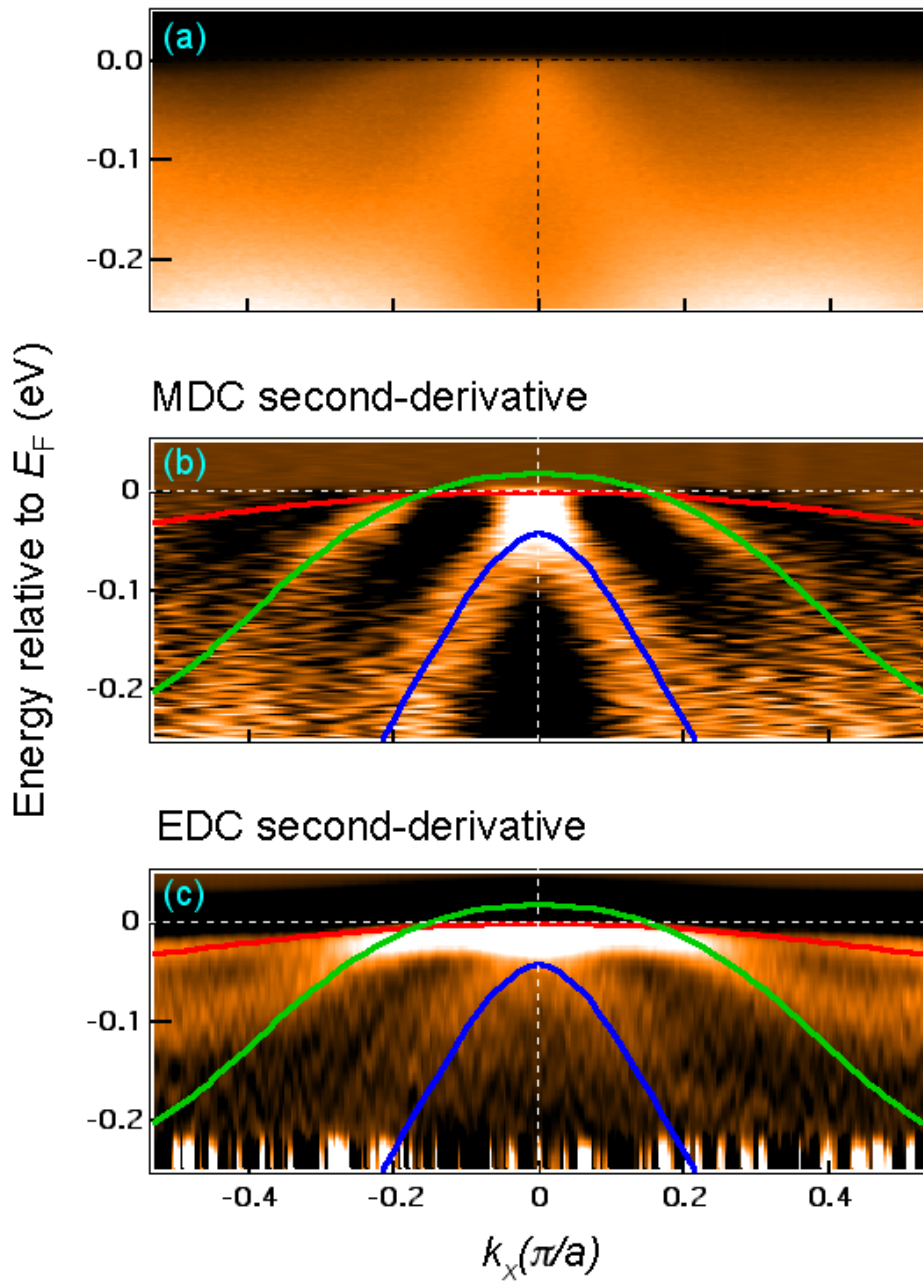
Fig. 5.2: (a) ARPES intensity plot of FeTe ($x = 0.1$) in the vicinity of E_F along the $\Gamma - M$ direction. (b), (c) Second-derivate plots of the ARPES spectra with respect to momentum and energy, respectively. The overlaid lines are calculated bands scaled with respect to energy to fit the experimental band dispersions.
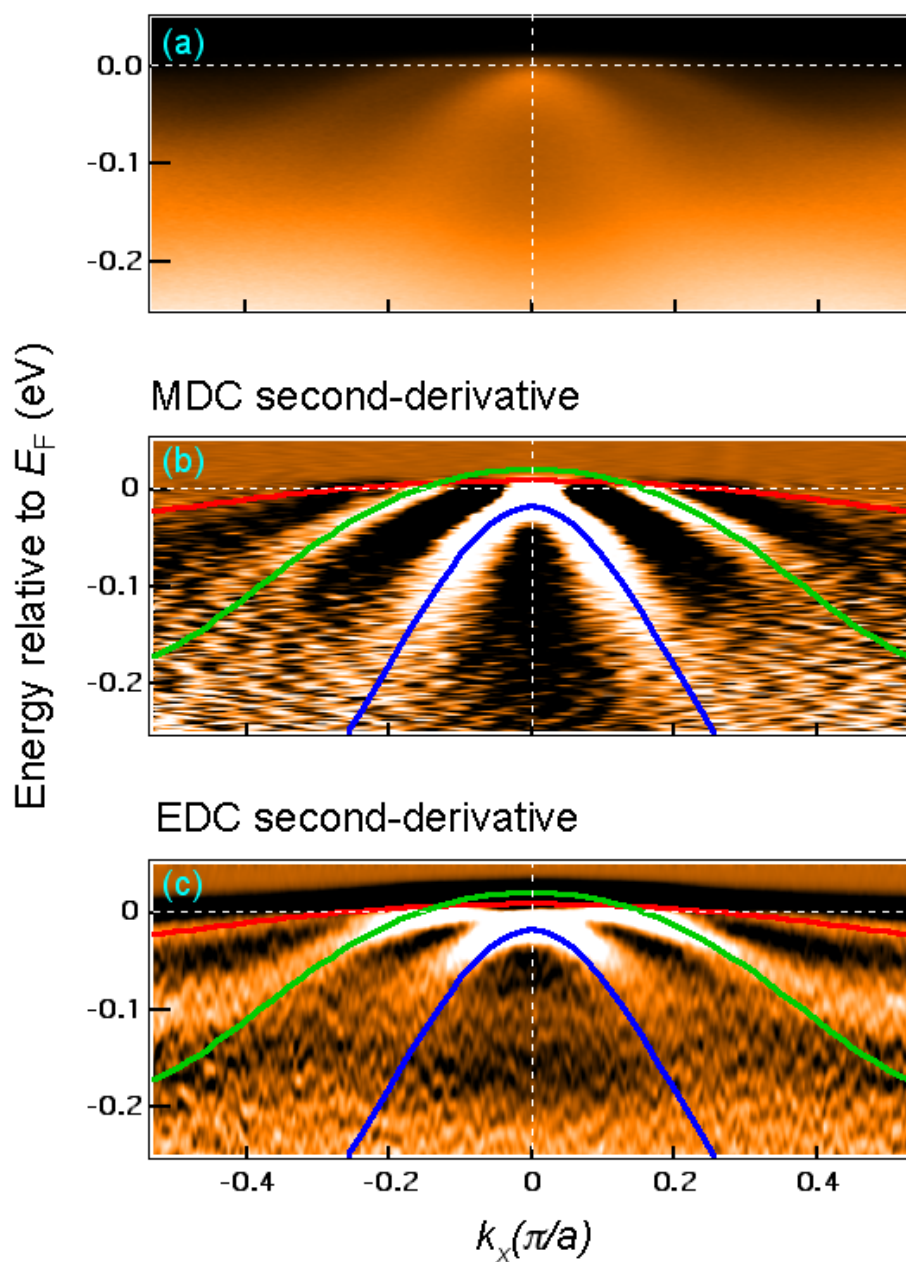
Fig. 5.3: (a) ARPES intensity plot of $FeTe_{0.8}Se_{0.2}$ ($x = 0.2$) in the vicinity of E_F along the $\Gamma - M$ direction. (b), (c) Second-derivate plots of the ARPES spectra with respect to momentum and energy, respectively. The overlaid lines are calculated bands scaled with respect to energy to fit the experimental band dispersions.

Fig. 5.4: (a) ARPES intensity plot of FeTe$_{0.6}$Se$_{0.4}$ (x = 0.4) in the vicinity of E_F along the $\Gamma - M$ direction. (b), (c) Second-derivate plots of the ARPES spectra with respect to momentum and energy, respectively. The overlaid lines are calculated bands scaled with respect to energy to fit the experimental band dispersions.

5.3.2 Mass renormalization

In order to compare the ARPES spectra with calculations, we have performed band structure calculations (courtesy of K. Okazaki) for FeTe using Wien2k package [56]. The result of the calculation is shown in Fig. 5.5 for various k_z values, which correspond to those expected for ARPES measurements with $hv = 22$ eV for each composition of $Fe_{1+y}Te_{1-x}Se_x$ ($x = 0$, 0.1, 0.2, and 0.4) from the c-axis lattice parameters taken from [57, 58] and the assumed inner potential of $V_0 = 12$ eV.

For the estimation of mass renormalization factors, we compared the calculated band structure at the corresponding k_z values to the experimental band dispersions. The calculated band dispersions are rescaled and shifted to match the MDC second-derivative image for d_{xz} and d_{yz} bands and EDC second-derivative image for d_{xy} band, respectively, because the band dispersions of each orbital are more clearly recognized for each image. The mass renormalization factors and the band shifts are tabulated in Table 5.2. From these results, we can see that the orbital dependence exists for the mass renormalization factor. The d_{xy} band is the most strongly renormalized with a mass renormalization factor of about 10. On the other hand, the other two orbitals of d_{xz} and d_{yz} have shown moderate electron correlation with almost the same value of around 1.5 - 2. This strong orbital differentiation of mass renormalization factor particularly in FeTe is largely due to its high chalcogen height, h, in fact the highest among the iron-based superconductors (see Fig. 4.1 (d) for the definition of chalcogen height). The chalcogen height controls the overlap of the Fe $3d$ and Se $4p$/Te $5p$ atoms and hence make Fe electrons more localized (itinerant) with increasing (decreasing) h. So far, the highest h is achieved in FeTe compound giving it the possibility to exhibit strongest electron correlation among iron-based materials.

In comparison with the DMFT + DFT calculation [13], our data agrees with it quantitatively as shown in Fig. 5.6(a). The obtained values are comparable to the calculated ones except for the d_{xz} and d_{yz}, which show relatively smaller values. Nevertheless, our results have provided systematic data for the $Fe_{1+y}Te_{1-x}Se_x$ compound showing that the compound is a strongly correlated material different from other iron-based superconductors. Moreover, our results further confirm the strong orbital dependence of the mass renormalization of $Fe_{1+y}Te_{1-x}Se_x$.

In terms of the composition dependence, only the d_{xz} band is strongly affected by the change in the Se concentration, which is evident in the band shift (see Fig. 5.6(b)). The other two bands, the d_{yz} and d_{xy} seem to be unaffected by the change in composition; both of their band positions and values of mass renormalization do not change with the change in Se concentration, as shown in Fig. 5.6. To understand the behavior of the d_{xz} band, we compare the result with our calculation. However, in our calculation (see Figure 5.5), the gap between the d_{xz} and d_{yz} orbitals increases with the increase in k_z showing an opposite trend with our data. This band shift cannot be accounted for from the difference in k_z, as what is reflected in our calculation, but maybe due largely to the change in the chalcogen height. In our calculation of k_z dispersion (courtesy of K. Okazaki) for FeTe and FeSe, shown in Figs. 5.6(c) and (d), respectively, the gap between the d_{xz} and d_{yz} bands is relatively wider in FeTe than in FeSe in the region of relevant k_z values around the midpoint of Γ and Z points. In addition, one can see that the d_{xz} band has a wider bandwidth and that the band top at the Γ point is located at a higher energy in FeTe than in FeSe which imply that the effect of Se substitution is to narrow the bandwidth and to push the band top towards higher energy, giving the overall effect of band shift towards higher energy.

Furthermore, the Fermi surface of the FeTe end of the $Fe_{1+y}Te_{1-x}Se_x$ compound is mostly consists of the largely enhanced d_{xy} band, which is

totally different from the FeSe end [29] where the d_{xy} band is buried in the deeper binding energy of around 50 meV. This behavior is actually consistent with the calculation [24] shown in Figs. 2.3(e) and (f). This result together with the unusually large orbital differentiation of mass renormalization in FeTe compound is the possible contributing factors for the disappearance of superconductivity in this compound.
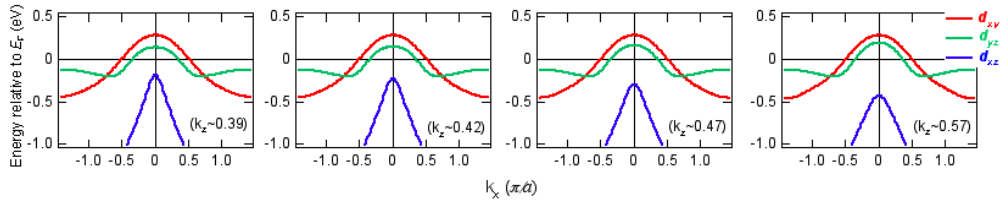

Fig. 5.5: FeTe LDA band structures for various k_z values (0.39, 0.42, 0.47 and 0.57 π/c) corresponding to those expected for ARPES measurements of the different compositions of $Fe_{1+y}Te_{1-x}Se_x$ (x = 0, 0.1, 0.2 and 0.4) with hv = 22 eV (Courtesy of K. Okazaki).
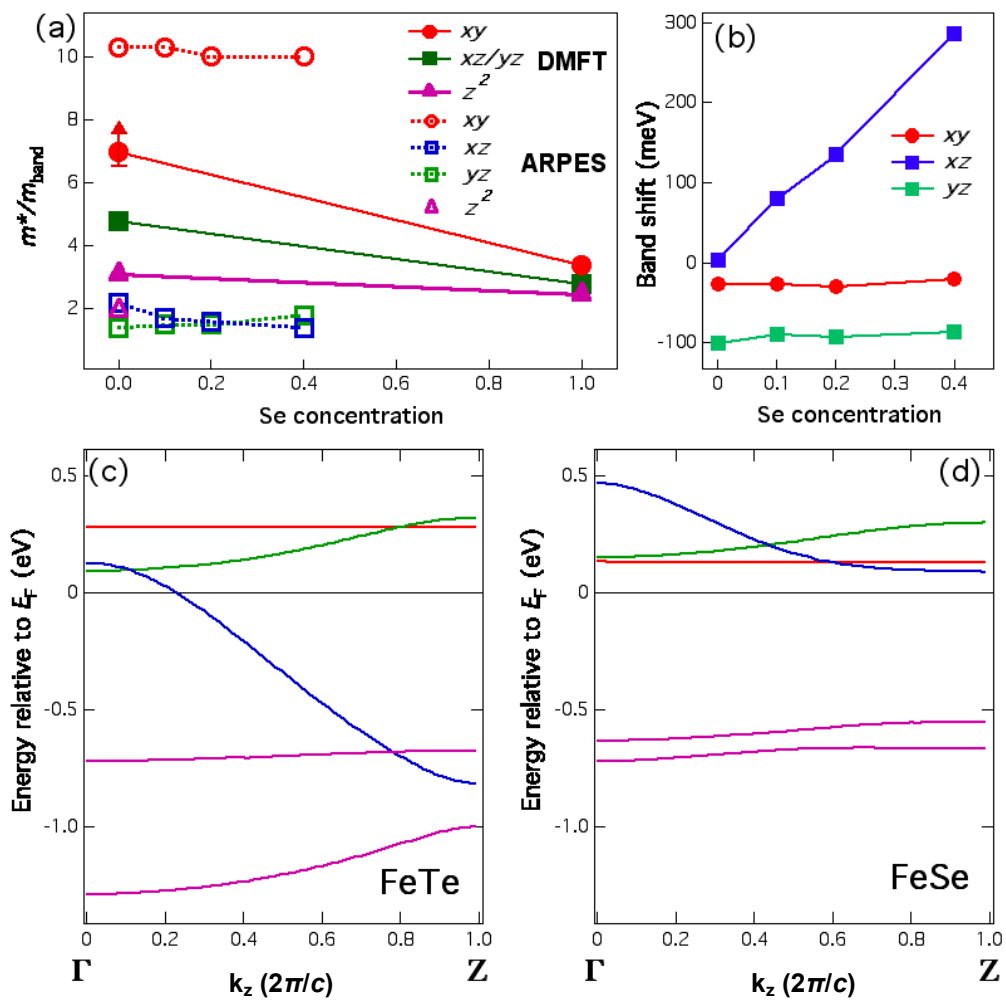
Fig. 5.6: (a) Comparison of the mass renormalization values with DMFT + DFT calculation [13]. (b) Band energy shift as a function of the Se content, x. (c), (d) k_z dispersion for FeTe and FeSe, respectively (Courtesy of K. Okazaki).

(x = 0) $Fe_{1.08}Te$	m^*/m_{band}	Band shift (meV)
d_{xy}	10.3	-27
d_{yz}	1.4	-100
d_{xz}	2.2	4
(x = 0.1) $Fe_{1.09}Te_{0.9}Se_{0.1}$		
d_{xy}	10.3	-27
d_{yz}	1.5	-90
d_{xz}	1.7	80
(x = 0.2) $Fe_{1.06}Te_{0.8}Se_{0.2}$		
d_{xy}	10.0	-30
d_{yz}	1.5	-93
d_{xz}	1.6	136
(x = 0.4) $FeTe_{0.6}Se_{0.4}$		
d_{xy}	10.0	-20
d_{yz}	1.8	-86
d_{xz}	1.4	286

Table 5.2: Values of mass renormalization and energy band shift obtained from rescaling of the energy of the calculated bands.

5.4 Conclusion

The mass renormalization factors obtained from photoemission measurements for the different bands of $Fe_{1+y}Te_{1-x}Se_x$ (x = 0, 0.1, 0.4, 1) are consistent with the DMFT + DFT calculation [13] and with other experimental data [29]. Our results provide additional evidence to further confirm the strong orbital dependence of the mass renormalization as well as the strong electron correlation in iron chalcogenides. Our results also provide a systematic data for $Fe_{1+y}Te_{1-x}Se_x$ that could help to resolve and clarify the inconsistencies and conflicting issues with other experimental data [24 – 28].

As with composition dependence, only the d_{xz} band exhibits strong Se concentration dependence as evident in the band shift. However, the other two bands, the d_{yz} and d_{xy} bands did not show significant changes in the band position, mass renormalization factor or strength of electron correlation. Furthermore, the unusually large orbital differentiation of mass renormalization for FeTe and the dominant contribution of the d_{xy} band on the Fermi surface maybe the contributing factors for the suppression of superconductivity on this compound.

66

Chapter 6

Summary

This research sought to investigate the electronic structure and to elucidate the strength of electron correlation in the simplest kind of iron-based superconductor, the $Fe_{1+y}Te_{1-x}Se_x$ system. For the first part, we carried out resonance photoemission experiments on the compounds, $x = 0, 0.4$ single crystals and polycrystalline FeSe ($x = 1$) samples, using photon energies in the Fe $3p \rightarrow 3d$ absorption region. We found out that, like most of the other iron-based superconductors, the density of states near the Fermi level down to the binding energy of around 2 eV is mostly dominated by the Fe $3d$ states. We also found out that the Fe $3p \rightarrow 3d$ resonance occurs at $hv \sim 55$ eV and we were able to deduce the Fe $3d$ partial density of states (PDOS) for all the samples. The near E_F peak structure in FeSe splits into two features in compounds with Te content. By comparing the PDOS with angle-resolved photoemission (ARPES) results, the peak structure can be attributed to the dominant Fe $3d_{z^2}$ states. We obtained the mass renormalization factor of around 2 for d_{z^2}, which shows moderate electron correlation consistent with the band calculation and previous photoemission results.

For the second part, we performed high-resolution ARPES measurements for the single crystals $Fe_{1+y}Te_{1-x}Se_x$ ($x = 0, 0.1, 0.2, 0.4$). Near the Fermi level, three band dispersions were clearly observed around the Γ point. The mass renormalization factors obtained from the ARPES measurements for the different bands are consistent with the DMFT + DFT calculation and have resolved inconsistencies and conflicting issues found in previous experimental data. Our results further confirm the strong orbital

dependence of the mass renormalization factor in iron chalcogenides and have shown that $Fe_{1+y}Te_{1-x}Se_x$ is a strongly correlated compound different from other iron-based superconductors. The d_{xy} band is the most strongly correlated with a mass renormalization factor of around 10, while the d_{yz} and d_{xz} bands show moderate electron correlations with mass renormalization factors of around 1.5 - 2. As for the composition dependence, only the d_{xz} band exhibits strong Se concentration dependence (chalcogen height-dependence) evident in the band shift, while the d_{yz} and d_{xy} bands did not show any significant change in the band position, nor in the mass renormalization factor or strength of electron correlation. The band shift of the d_{xz} orbital is due to its strong dependence on the chalcogen height as well as on the k_z dispersion especially around the k_z values relevant to our study.

In conclusion, using photoemission spectroscopy, which is a powerful tool to investigate the electronic structure of solids, we have found that the simplest iron-based superconductor $Fe_{1+y}Te_{1-x}Se_x$ is a strongly correlated material different from other iron-based superconductors. The unusually large orbital differentiation of mass renormalization factor for this compound, particularly for FeTe, and the dominant contribution of the largely enhanced d_{xy} band on the Fermi surface are possible contributing factors for the suppression of superconductivity on this compound.

Acknowledgment

It is my great pleasure to express my sincere gratitude to everyone who has been with me since I started my graduate studies here in Japan.

I thank the ALMIGHTY GOD for the strength and guidance He has given me all these years to continue my studies here in The University of Tokyo. Without Him, I am nothing. I am always and forever grateful to Him.

This thesis would not have been possible if not for my wife, Rose and my son, Clint, who have always been my constant support and encouragement. You have always been a source of inspiration whenever I am about to break. I am also grateful to my parents, brothers and sisters, for the encouragement and support for whatever undertakings I take. Thank you for always being there for me.

The results of my experiments and my progress as a student would not have reached its completion without the support and guidance of my adviser, Prof. Atsushi Fujimori. He has never gave up on me even though there are a lot of times I almost gave up on myself. I am so honored to be under his tutelage. I express my sincere gratitude to you, Sensei.

I am truly indebted to Dr. Teppei Yoshida and Dr. Kozo Okazaki, for teaching me the principle of photoemission and for mentoring me the experimental techniques during beamtime. I have learned a lot from you especially on the analysis of my data. I am especially grateful to Dr. Kozo Okazaki for the Wien2k calculations, which are very vital in my analysis.

I am thankful to my thesis examiners, Prof. Kouji Taniguchi, Prof. Shuji Hasegawa, Prof. Masashi Takigawa, Prof. Yasutami Takada and Prof. Toshiro Sakakibara, for taking their time to review my work. They have contributed a number of valuable comments and suggestions for the improvement of this study.

regarding my life as a foreign student, facilitating all my transactions from the start even before I came to Japan. You have helped my student life easier.

Furthermore, I am really thankful for the opportunity afforded for me by the University of Tokyo. My 4-years stay in the university was really an exciting and fulfilling one. I am also thankful for the Monbukagakusho (MEXT) scholarship through the Embassy of Japan in the Philippines. My sincere thanks for the financial assistance you have given me for my studies. It really helped me a lot. I am also equally thankful to Mindanao State University – Iligan Institute of Technology (MSU-IIT), for granting me study leave through the Faculty Development Program (FDP).

I am also thankful to my Todai Filipino students (todaipips) friends, thanks for your company. Thanks for the many sporadic tea times we had. Thanks for those priceless laughs during those great meals.

And to the unsung individuals who have helped me in this study and those who kept my esteem high when everything seems so wrong, thank you very much.

Leo Cristobal C. Ambolode II
Tokyo, 2014

References

[1] H. K. Onnes, *Proc*. 11 (1909) 168, *Comm*. 108 (1908).

[2] H. K. Onnes: Leiden Comm. (1911) 120b, 122c, 124c.

[3] J. G. Bednorz and K. A. Müller: Z. Phys. B **64**, 189 (1986).

[4] Y. Kamihara, T. Watanabe, M. Hirano, and H. Hosono, *J. Am. Chem. Soc.* **130**, 3296 (2008).

[5] F. Bloch, Z. Phys. **52**, 555 (1928).

[6] A. H. Wilson, Proc. Roy. Soc. A **133**, 458 (1931).

[7]. J. H. de Boer, and E. J. W. Verway, Proc. Phys. Soc. London, Sect. A **42**, 59 (1937).

[8] N. F. Mott, Proc. Roy. Soc. A **62**, 416 (1949).

[9] J. Hubbard, Proc. Soc. A **277**, 237 (1964).

[10] J. Hubbard, Proc. Soc. A **281**, 401 (1964).

[11] P. W. Anderson, Phys. Rev. **115**, 2 (1959).

[12] P. W. Anderson, Solid State Phys. **14**, 99 (1963).

[13] Z. P. Yin, K. Haule, and G. Kotliar*,* Nature Mater. **10**, 932 (2011).

[14] J. W. Lynn, and P. Dai, Physica C **469**, 469 (2009)

[15] J. Paglione and R. L. Greene, Nature Phys. **6**, 645 (2010).

[16] C. Wang, L. Li, S. Chi, Z. Zhu, Z. Ren, Y. Li, Y. Wang, X. Lin, Y. Luo,

74

S. Jiang, Z. Xu, G. Cao, and Z. Xu: Euro Phys. Lett. **83**, 67006 (2008).

[17] M. Rotter, M. Tegel, I. Shellenberg, W. Hermes, R. Pottgen, and D. Johrendt, Phys. Rev. B **78**, 020503 (2008).

[18] M. Rotter, M. Tegel, and D. Johrendt, Phys. Rev. Lett. **101**, 107006 (2008).

[19] X.C. Wang, Q.Q. Liu, Y.X. Lv, W.B. Gao, L.X. Yang, R.C. Yu, F.Y. Li, C.Q. Jin, *Solid State Communications* **148**, 538 (2008).

[20] F.-C. Hsu, J.-Y. Luo, K.-W. Yeh, T.-K. Chen, T.-W. Huang, P. M. Wu, Y.-C. Lee, Y.-L. Huang, Y.-Y. Chu, D.-C. Yan, and M.-K. Wu, Proc. Natl. Acad. Sci. USA **105**, 14262 (2008).

[21] X. Zhu, F. Han, G. Mu, P. Cheng, B. Shen, B. Zeng, and H.-H Wen, arXiv: 0904:1732 (2009).

[22] N. Katayama, S. Ji, D. Louca, S. Lee, M. Fujita, T. J. Sato, J. Wen, Z. Xu, G. Gu, G. X, Z. Lin, M. Enoki, S. Chang, K. Yamada, and J. M. Tranquada, J. Phys. Soc. Japan **79**, 112702 (2010).

[23] A. Subedi, L. Zhang, D. J. Singh and M. H. Du*,* Phys. Rev. B **78**, 134514 (2008).

[24] A. Tamai, A. Y. Ganin, E Rozbicki, J. Bacsa, W. Meevasana, P. D. C. King, M. Caffio, R. Schaub, S. Margadonna, K. Prassides, M. J. Rossiensky, and F. Baumberger, Phys. Rev. Lett. **104**, 097002 (2010).

[25] Y. Zhang, F. Chen, C. He, L. X. Yang, B. P. Xie, Y. L. Xie, X. H. Chen, M. Fang, M. Arita, K. Shimada, H. Namatame, M. Taniguchi, J. P. Hu, and D. L. Feng, Phys. Rev. B **82**, 165113 (2010).

[26] Y. Xia, D. Qian, L. Wray, D. Hsieh, G. F. Chen, J. L. Luo, N. L. Wang, and M. Z. Hasan, Phys. Rev. Lett. **103**, 037002 (2009).

[27] K. Nakayama, T. Sato, P. Richard, T. Kawahara, Y. Sekiba, T. Qian, G. F. Chen, J. L. Luo, N. L. Wang, H. Ding, and T. Takahashi, Phys. Rev. Lett. **105**, 197001 (2010).

[28] F. Chen, B. Zhou, Y. Zhang, J. Wei, H.-W. Ou, J.-F. Zhao, C. He, Q.-Q. Ge, M. Arita, K. Shimada, H. Namatame, M. Taniguchi, Z.-Y. Lu, J. Hu, X.-Y. Cui, and D. L. Feng, Phys. Rev. B **81**, 014526 (2010).

[29] J. Maletz, V. B. Zabolotnyy, D. V. Evtushinsky, S. Thirupathaiah, A. U. B. Wolter, L. Harnagea, A. N.Yaresko, A. N.Vasiliev, D. A. Chareev, E. D. L. Rienks, B. Büchner, and S. V. Borisenko, arXiv:1307.1280.

[30] A. Damascelli, Z. Hussain, and Z.-X. Shen, Rev. Mod. Phys. **75**, 473 (2003).

[31] S. Hufner, Photoelectron Spectroscopy (Springer, Berlin, 1996)

[32] A. C. R. Brundle, J. Vac. Sci. Technol., **212** (1974).

[33] U. Fano, Phys. Rev. **124**, 1866 (1961).

[34] Ren Zhi-An, Lu Wei, Yang Jie, Yi Wei, Shen Xiao-Li, Zheng-Cai, Che Guang-Can, Dong Xiao-Li, Sun Li-Ling, Zhou Fang and Zhao Zhong-Xian, *Chinese Phys. Lett.* **25**, 2215 (2008).

[35] S. Margadonna, Y. Takabayashi, Y. Ohishi, Y. Mizuguchi, Y. Takano, T. Kagayama, T. Nakagawa, M. Takata and K. Prassides, Phys. Rev. B **80**, 064506 (2009).

[36] S. Medvedev, T. M. McQueen, I. A. Troyan, T. Palasyuk, M. I. Eremets,

R. J. Cava, S. Naghavi, F. Casper, V. Ksenofontov, G. Wortmann and C. Felser, Nature Mater. **8**, 630 (2009).

[37] Q.-Y. Wang, Z. Li, W.-H. Zhang, Z.-C. Zhang, J.-S. Zhang, W. Li, H. Ding, Y. B. Ou, P. Deng, K. Chang, J. Wen, C.-l. Song, K. He, J.-f. Jia, S.-H. Ji, Y.-Y. Wang, L. Wang, X. Chen, X.-C. Ma, and Q.-k. Xue, *Chinese Physics Letters* **29**, 037402 (2012).

[38] S. He, J. He, W. Zhang, L. Zhao, D. Liu, X. Liu, D. Mou, Y.-B. Ou, Q.-Y. Wang, Z. Li, L. Wang, Y. Peng, Y. Liu, C. Chen, L. Yu, G. Liu, X. Dong, J. Zhang, C. Chen, Z. Xu, X. Chen, X. Ma, Q. Xue, and X. J. Zhou, arXiv:1207.6823.

[39] M. H. Fang, H. M. Pham, B. Qian, T. J. Liu, E. K. Vehstedt, Y. Liu, L. Spinu, and Z. Q. Mao, Phys. Rev. B **78**, 1 (2008).

[40] C.-Y. Moon and H. J. Choi, Phys. Rev. Lett. **104**, 057003 (2010).

[41] R. Khasanov, M. Bendele, A. Amato, P. Babkevich, a. T. Boothroyd, A. Cervellino, K. Conder, S. N. Gvasaliya, H. Keller, H.-H. Klauss, H. Luetkens, V. Pomjakushin, E. Pomjakushina, and B. Roessli, Phys. Rev. B **80**, 2 (2009).

[42] K.-W. Yeh, T.-W. Huang, Y.-l. Huang, T.-K. Chen, F.- C. Hsu, P. M. Wu, Y.-C. Lee, Y.-Y. Chu, C.-L. Chen, J.-Y. Luo, D.-C. Yan, and M.-K. Wu, Euro. Phys. Lett. **84**, 37002 (2008).

[43] J. Wen, G. Xu, G. Gu, J. M. Tranquada, and R. J. Birgeneau, Rep. Prog. Phys. **74**, 124503 (2011).

[44] R. Yoshida, T. Wakita, H. Okazaki, Y. Mizuguchi, S. Tsuda, Y. Takano, H. Takeya, K. Hirata, T. Muro, M. Okawa, K. Ishizaka, S. Shin, H. Harima, M. Hirai, Y. Muraoka, and T. Yokoya, J. Phys. Soc. Japan **78**, 034708 (2009).

[45] A. Yamasaki, Y. Matsui, S. Imada, K. Takase, H. Azuma, T. Muro, Y. Kato, A, Higashiya, A. Sekiyama, S. Suga, M. Yabashi, K. Tamasaku, T. Ishikawa, K. Terashima, H. Kobori, A. Sugimura, N. Umeyama, H. Sato, Y. Hara, N. Miyagawa and S. Ikeda, Phys. Rev. B **82**, 184511 (2010).

[46] T. Yokoya, R. Yoshida, Y. Utsumi, K. Tsubota, H. Okazaki, T. Wakita, Y. Mizuguchi, Y. Takano, T. Muro, Y. Kato, H. Kumigashira, M. Oshima, H. Harima, Y. Aiura, H. Sato, A. Ino, H. Namatame, M. Taniguchi, M. Hirai and Y. Muraoka, Sci. Technol. Adv. Mater. **13**, 054403 (2012).

[47] M. Aichhorn, S. Biermann, T. Miyake, A. Georges and M. Imada, Physical Review B **82**, 064504 (2010).

[48] H.-J. Hagemann, W. Gudat and C. Kunz, Journal of the Optical Society of America **6**, 65 (1975).

[49] W. Malaeb, T. Yoshida, T. Kataoka, A. Fujimori, M. Kubota, K. Ono, H. Usui, K. Kuroki, R. Arita, H. Aoki, Y. Kamihara, M. Hirano, and H. Hosono, J. Phys. Soc. Japan **77**, 093714 (2008).

[50] A. Georges, G. Kotliar, W. Krauth, and M. J. Rozenberg, Rev. of Mod. Phys. **68**, (1996).

[51] A. Georges, L. d. Medici, and J. Mravlje, arXiv:1207.3033 (2012).

[52] S. Li, C. dl. Cruz, Q. Huang, Y. Chen, J. W. Lynn, J. Hu, Y.-L. Huang, F.-C Hsu, K.-W. Yeh, M.-K. Wu, and P. Dai, Phys. Rev. B **79**, 054503 (2009).

[53] Y. Mizuguchi and Y. Takano, J. Phys. Soc. Japan **79**, 102001 (2010).

[54] Y. Lubashevsky, E. Lahoud, K. Chashka, D. Podolsky and A. Kanigel, Nature Phys. **8**, 309 (2012).

[55] H. Miao, P. Richard, Y. Tanaka, K. Nakayama, T. Qian, K. Umezawa, T. Sato, Y.-M. Xu, Y. B. Shi, N. Xu, X.-P. Wang, P. Zhang, H.-B. Yang, Z.-J. Xu, J. S. Wen, G.-D. Gu, X. Dai, J.-P. Hu, T. Takahashi, and H. Ding, Phys. Rev. B **85**, 094506 (2012).

[56] P. Blaha, K. Schwarz, G.K.H. Madsen, D. Kvasnicka, J. Luitz, WIEN2k, An Augmented Plane Wave Plus Local Orbitals Program for Calculating Crystal Properties, Vienna University of Technology, Austria, 2001.

[57] T. Miyake, K. Nakamura, R. Arita, and M. Imada, J. Phys. Soc. Japan, **79**, 044705 (2010).

[58] M. H. Fang, M. H. Pham, B. Qian, T. J. Liu, E. K. Vehstedt, Y. Liu, L. Spinu, and Z. Q. Mao, Phys. Rev. B **78**, 224503 (2008).